

Gravitational waves from eccentric extreme mass-ratio inspirals as probes of scalar fields

Chao Zhang,^a Yungui Gong,^{b,1} Dicong Liang,^c and Bin Wang^{d,e}

^aSchool of Physics and Astronomy, Shanghai Jiao Tong University, 800 Dongchuan Rd, Shanghai 200240, China

^bSchool of Physics, Huazhong University of Science and Technology, 1037 LuoYu Rd, Wuhan, Hubei 430074, China

^cKavli Institute for Astronomy and Astrophysics, Peking University, No.5 Yiheyuan Road , Beijing 100871, China

^dCenter for Gravitation and Cosmology, Yangzhou University, 88 South Daxue Rd, Yangzhou, Jiangsu 225009, China

^eSchool of Aeronautics and Astronautics, 800 Dongchuan Rd, Shanghai 200240, China

E-mail: zhangchao666@sjtu.edu.cn, yggong@hust.edu.cn, dcliang@pku.edu.cn, wang_b@sjtu.edu.cn

Abstract. We study eccentric orbits of the Schwarzschild spacetime for extreme mass ratio system (EMRI) in modified gravity theories with additional scalar fields. Due to the additional energy and angular momentum carried away by the scalar field, the orbit of the EMRI in modified gravity decays faster than that in general relativity. The time that it takes the eccentricity e to reach the minimum is shorter and the values of the semi-latus rectum p and e at the turning point when e reaches the minimum are bigger for larger scalar charge d . In addition to the calculation of energy fluxes with numerical methods, we also use the Post-Newtonian expansion of the rate of energy carried away by the scalar field in eccentric orbits to understand the behaviors of the energy emission. By adding the scalar flux to the open code FastEMRIWaveforms of the Black Hole Perturbation Toolkit, we numerically generate fast gravitational waveforms for eccentric EMRIs with scalar fields and use the faithfulness between waveforms with and without the scalar charge to discuss the detection of scalar charge d . The detection error of the scalar charge is also estimated with the method of the Fisher information matrix.

Keywords: gravitational waves, EMRIs, scalar charge

¹Corresponding author.

Contents

| | | |
|----------|--|-----------|
| 1 | Introduction | 1 |
| 2 | Theoretical framework | 3 |
| 3 | Orbital evolution and waveform | 5 |
| 4 | Numerical results | 8 |
| 5 | Analytical results | 11 |
| 6 | Parameter estimation | 16 |
| 7 | Conclusions | 17 |
| A | Comparison of Fisher information matrix of the Schwarchild case and Kerr case | 20 |

1 Introduction

In 2015 the Laser Interferometer Gravitational-Wave Observatory (LIGO) Scientific Collaboration and the Virgo Collaboration directly detect the first gravitational wave (GW) event GW150914 [1, 2], this opens a new window to understand the nature of gravity in the nonlinear and strong field regimes. So far there have been tens of confirmed GW detections [3–6]. However, the ground-based GW observatories can measure GWs in the frequency range $10 - 10^3$ Hz only, due to the seismic and gravity gradient noises, which means that a wealth of astrophysical signals in the lower frequency ranges $10^{-4} - 10^{-1}$ Hz are difficult to be explored. Extreme mass ratio inspirals (EMRIs) composed of a stellar-mass object inspiraling into a supermassive black hole (SMBH) with masses in the range of $10^6 - 10^9 M_\odot$ [7], emitting GWs in the milli-Hertz band, are the most promising GW sources for space-based observatories like the Laser Interferometer Space Antenna (LISA) [8, 9], TianQin [10] and Taiji [11, 12]. GW signals from EMRIs provide highly accurate information about the parameters and orbits of the system which enable us to constrain additional gravitational fields in alternative theories of gravity [13–20].

In the framework of Einstein’s general relativity (GR), GWs have tensor polarizations only and quadrupolar radiation is the lowest mode, while additional polarizations and emission channels might exist in alternative theories of gravity [21, 22]. For example, in scalar-tensor theories such as Brans-Dicke (BD) theory [21, 23, 24], there exists the scalar dipolar radiation in quasicircular orbits [25, 25–29]. In addition to the dipolar emission, monopolar radiation also presents if the eccentricity is nonzero [30, 31], such additional emission channels in BD theory for eccentric binaries can be helpful to distinguish BD theory from GR. The detection of eccentric binaries and the measurement of the eccentricity are not only useful to infer the binary formation mechanism [32–41], but also helpful to constrain alternative theories of gravity. Although the strength of the scalar mode is not comparable with those of the tensor modes, there are still cumulative effects that can be detected by the space-based detectors [13, 14, 21, 22, 25, 30, 42–48]. The black hole (BH) endowed with the additional

scalar field can carry a scalar charge whose quantity is inverse to the mass squared in a class of scalar-tensor theories [49–60]. Different theories and models may have different constraints on the scalar charge. A notable example is (decoupled) Einstein-dilaton Gauss-Bonnet gravity [29, 60], the scalar charge-to-mass ratio d of the BH is proportional to the dimensionless coupling constant of the theory $\beta = 2\alpha/\text{mass}^2$, specifically $d = 2\beta + (73/15)\beta^3$ [61]. The constant α with a unit of $(\text{length})^2$ describes the coupling between quadratic-in-curvature scalars and a massless scalar field. For the existence of the stable BH, the charge d should be less than 0.572 [62]. The constraint through the Shapiro time delay using the Saturn probe Cassini on $\sqrt{\alpha}$ is limited below 8.9×10^6 km [63]. The low-mass x-ray binary GRO J0422+32 [51] and A0620-00 [64] constrain the $\sqrt{\alpha}$ below 3.1 km and 1.9 km, respectively. This new constraint is more than six orders of magnitude stronger than the solar system bound. The strongest constraint from the Bayesian analysis on GW190814, assuming it is a BBH merger, is $\sqrt{\alpha} \leq 5.6$ km for using GWTC-1 [60], $\sqrt{\alpha} \leq 0.4$ km for using GWTC-2 [65] and $\sqrt{\alpha} \leq 0.27$ km for using GWTC-3 [66] at 90% credibility. If GW190814 is not a BH binary, then the strongest constraint comes from GW 200115, giving $\sqrt{\alpha} \leq 1.1$ km [66], which corresponds to $d \leq 0.022$ for the BH with mass $10 M_\odot$.

For EMRIs, the radiation reaction acting on the test particle can be split into two parts: the dissipative one and the conservative one. When the motion of the test particle is geodesic over a time scale comparable to the orbital period, we can consider the dissipative part under the adiabatic approximation only. The dissipative part can be calculated from the energy and angular momentum flux at the horizon of the central BH and at infinity. The method of calculating the effects of radiation reaction on the bound orbits in the Schwarzschild space-time is based on the Teukolsky formalism for BH perturbations [67–71]. A more detailed presentation can be found in [72–75]. When the adiabatic approximation is valid, the calculation proceeds as follows [75]. Assuming that the motion is strictly geodesic over several orbital periods, we calculate the energy and angular momentum flux from the system and then give the time-averaged rates of change of the orbital parameters. Then we derive the orbital evolutions for the semi-latus rectum p and the eccentricity e from the initial conditions. As pointed in Ref. [75], as long as the extreme mass ratio is suitably satisfied, the results are compatible with the initial assumption, and the calculation is self-consistent.

Maselli et al. discussed the possible detection of scalar fields with EMRIs onto Schwarzschild BHs in circular orbits by LISA and they found that the accumulated dephasing due to the scalar charge of the small body with four-year observations of EMRIs can be detected [13]. By calculating the difference in the number of GW cycles accumulated by EMRIs on circular orbits with the mass $\mu = 10M_\odot$ for the small body, they found that the smaller mass the supermassive BH, the smaller the scalar charge d detectable [13]. Then the analysis was extended to EMRIs onto $10^6 M_\odot$ Kerr BHs with the dimensionless spin $\chi = 0.9$ in circular orbits [14]. It was found that with one-year observation, LISA could detect the scalar charge d as small as $d \sim 5 \times 10^{-3}$ and $d \gtrsim 0.01$ by the dephasing and faithfulness between two GWs with and without the scalar charge, respectively [14]. Using the Fisher information matrix (FIM) method, one-year observation of EMRIs with a signal-to-noise ratio (SNR) of 150, LISA could constrain the scalar charge as small as $d \sim 0.05$ to be inconsistent with zero at the 3σ confidence level and the scalar charge is highly correlated with the mass of the small compact object and anti-correlated with the spin parameter and the mass of the central Kerr BH [14]. Barsanti et al. numerically calculated the evolution of eccentric orbits in Kerr spacetime and they discussed how the scalar charge affects the orbital evolution for different eccentricities and different values of the BH spin, they also discussed the effects of

the scalar charge and the eccentricity on the dephasing and faithfulness between signals with and without the scalar charge, and they found that the eccentricity improves the detectability of the scalar charge, at least for $d \gtrsim 0.01$ [76]. Since more massive Schwarzschild BH in circular EMRIs improves the distinguishability of the scalar charge while massive Kerr BH decreases the distinguishability of the scalar charge, can the eccentricity affect the dependence of the detectability of the scalar charge on the mass of the Schwarzschild BH? In this paper, we address this problem by calculating GWs in eccentric orbits and by using the Fisher information matrix to estimate the errors of detecting the scalar charge. We also use the post-Newtonian expansion of GW emission by the scalar field to understand the numerical results and evaluate factors that influence the detectability of the scalar field. Furthermore, based on the open code FastEMRIWaveforms [77], we add the energy flux emitted by scalar fields to generate fast GW waveforms for eccentric EMRIs. In Sec. 2, we introduce the background of the model and the Teukolsky perturbation formalism. In Sec. 3, we calculate the source of the Teukolsky equation and orbital evolution equations as well as waveforms. In Sec. 4, we give the numerical results of orbital evolution and waveform. In Sec. 5, we give the analytical results of energy rates. In Sec. 6, we use the modified FastEMRIWaveforms to generate GW waveforms and perform the Fisher information matrix to estimate the errors of detecting scalar charge. The last section is devoted to conclusions and discussions.

2 Theoretical framework

In this section, we consider a general action [13]

$$S[\mathbf{g}, \varphi, \Psi] = S_0[\mathbf{g}, \varphi] + \alpha S_c[\mathbf{g}, \varphi] + S_m[\mathbf{g}, \varphi, \Psi], \quad (2.1)$$

where

$$S_0 = \int d^4x \frac{\sqrt{-g}}{16\pi} \left(R - \frac{1}{2} \partial_\mu \varphi \partial^\mu \varphi \right), \quad (2.2)$$

R is the Ricci scalar and φ is a massless scalar field. The nonminimal coupling between the metric tensor \mathbf{g} and the scalar field φ is denoted by the term αS_c and the coupling constant α has the dimension $[\alpha] = (\text{mass})^n$ with $n > 0$. In the skeletonized approach [42, 78–80], the secondary body in an EMRI is treated as a point particle, the matter action S_m for the secondary body reads

$$S_m[\mathbf{g}, \varphi, \Psi] = - \int m(\varphi) d\tau, \quad (2.3)$$

where τ denotes the proper time and the mass $m(\varphi)$ of the point particle depends on the value of the scalar field at the location of the particle. Varying the action with respect to the metric tensor and the scalar field yields

$$G^{\mu\nu} = R^{\mu\nu} - \frac{1}{2} g^{\mu\nu} R = T_{\text{scal}}^{\mu\nu} + \alpha T_c^{\mu\nu} + 8\pi T_p^{\mu\nu}, \quad (2.4)$$

$$\square\varphi + \frac{16\pi\alpha}{\sqrt{-g}} \frac{\delta S_c}{\delta\varphi} = 16\pi \int m'(\varphi) \frac{\delta^{(4)}(x - y(\tau))}{\sqrt{-g}} d\tau, \quad (2.5)$$

where

$$T_{\text{scal}}^{\mu\nu} = \frac{1}{2} \partial^\mu \varphi \partial^\nu \varphi - \frac{1}{4} g^{\mu\nu} g_{\alpha\beta} \partial^\alpha \varphi \partial^\beta \varphi, \quad (2.6)$$

$$T_c^{\mu\nu} = - \frac{16\pi}{\sqrt{-g}} \frac{\delta S_c}{\delta g^{\mu\nu}}, \quad (2.7)$$

$$T_p^{\mu\nu} = \int m(\varphi) \frac{\delta^{(4)}(x - y(\tau))}{\sqrt{-g}} \frac{dy^\mu}{d\tau} \frac{dy^\nu}{d\tau} d\tau, \quad (2.8)$$

$m'(\varphi) = dm(\varphi)/d\varphi$, x describes the spacetime point and $y(\tau)$ is the particle's worldline. We consider the inspiral of a small BH into a massive Schwarzschild BH with the extreme mass ratio between the small body and the central BH. In theories like the scalar Gauss-Bonnet (sGB) gravity, the small BH carries a scalar charge. If the conditions $\alpha T_c^{\mu\nu} \ll G^{\mu\nu}$ and $\alpha \frac{\delta S_c}{\delta \varphi} \ll \square \varphi$ are satisfied, then Einstein's equation and the scalar field equation for EMRIs reduce to [13]

$$G^{\mu\nu} \approx 8\pi T_p^{\mu\nu} = 8\pi m_p \int \frac{\delta^{(4)}(x - y(\tau))}{\sqrt{-g}} \frac{dy^\mu}{d\tau} \frac{dy^\nu}{d\tau} d\tau, \quad (2.9)$$

$$\square \varphi = S = 4\pi m_p d \int \frac{\delta^{(4)}(x - y(\tau))}{\sqrt{-g}} d\tau, \quad (2.10)$$

where $m_p = m(\varphi_0)$, $d = 4m'(\varphi_0)/m(\varphi_0)$ is the dimensionless scalar charge of the small BH and φ_0 stands for the background value of the scalar field. The primary BH provides an approximate Schwarzschild background. In the Teukolsky formalism, the Newman-Penrose scalar Ψ_4 and the scalar perturbation φ are decomposed into spherical harmonic components as follows

$$\begin{aligned} \Psi_4 &= \int_{-\infty}^{+\infty} d\omega \sum_{lm} r^{-4} R_{\omega lm}(r) {}_{-2}Y_{lm}(\theta, \phi) e^{-i\omega t}, \\ \varphi &= \int_{-\infty}^{+\infty} d\omega \sum_{lm} r^{-1} X_{\omega lm}(r) {}_0Y_{lm}(\theta, \phi) e^{-i\omega t}, \end{aligned} \quad (2.11)$$

where ${}_sY_{lm}(\theta, \phi)$ is the spin-weighted spherical harmonics. The radial functions $R_{\omega lm}(r)$ and $X_{\omega lm}(r)$ satisfy the inhomogeneous Teukolsky equation

$$\begin{aligned} \left[r^2 f \frac{d^2}{dr^2} - 2(r - M) \frac{d}{dr} + U_1(r) \right] R_{\omega lm}(r) &= -T_{\omega lm}(r), \\ \left[f^2 \frac{d^2}{dr^2} + \frac{2Mf}{r^2} \frac{d}{dr} + U_2(r) \right] X_{\omega lm}(r) &= -S_{\omega lm}(r), \end{aligned} \quad (2.12)$$

where $f = 1 - 2M/r$, M is the mass of the central BH and

$$\begin{aligned} U_1(r) &= f^{-1} (\omega^2 r^2 - 4i\omega(r - 3M)) - (l - 1)(l + 2), \\ U_2(r) &= \omega^2 - r^{-2} f \left(l(l + 1) + \frac{2M}{r} \right). \end{aligned} \quad (2.13)$$

The source term in Eq. (2.12) is

$$S_{\omega lm}(r) = \frac{1}{2\pi} \int dt d\Omega r f S {}_0\bar{Y}_{l,m}(\theta, \phi) e^{i\omega t}, \quad (2.14)$$

S will be given below and $T_{\omega lm}$ is given in [75]. The homogeneous Teukolsky equation admits two linearly independent solutions $X_{lm\omega}^{\text{in}}$ and $X_{lm\omega}^{\text{up}}$, with the following asymptotic values at the horizon $r = 2M$ and at infinity,

$$X_{lm\omega}^{\text{in}} = \begin{cases} e^{-i\omega r^*}, & (r^* \rightarrow -\infty) \\ A_{\text{out}} e^{i\omega r^*} + A_{\text{in}} e^{-i\omega r^*}, & (r^* \rightarrow +\infty) \end{cases} \quad (2.15)$$

$$X_{lm\omega}^{\text{up}} = \begin{cases} B_{\text{up}} e^{i\omega r^*} + B_{\text{in}} e^{-i\omega r^*}, & (r^* \rightarrow -\infty) \\ e^{i\omega r^*}, & (r^* \rightarrow +\infty) \end{cases} \quad (2.16)$$

where the tortoise radius $r^* = r + 2M \ln(r/2M - 1)$. The solutions $X_{lm\omega}^{\text{in}}$ and $X_{lm\omega}^{\text{up}}$ are purely outgoing at infinity and purely ingoing at the horizon. With the help of these homogeneous solutions, the solution to Eq. (2.12) is

$$X(r) = \frac{X_{lm\omega}^{\text{in}} \int_{r^*}^{+\infty} S_{lm\omega} X_{lm\omega}^{\text{up}} dr^* + X_{lm\omega}^{\text{up}} \int_{-\infty}^{r^*} S_{lm\omega} X_{lm\omega}^{\text{in}} dr^*}{W}, \quad (2.17)$$

where the Wronskian of $X_{lm\omega}^{\text{in}}$ and $X_{lm\omega}^{\text{up}}$ is

$$W = X_{lm\omega}^{\text{in}} \frac{dX_{lm\omega}^{\text{up}}}{dr^*} - X_{lm\omega}^{\text{up}} \frac{dX_{lm\omega}^{\text{in}}}{dr^*} = 2i\omega A_{\text{in}}. \quad (2.18)$$

3 Orbital evolution and waveform

The timelike geodesics of the Schwarzschild spacetime on the equatorial plane $\theta = \pi/2$ are described by the equations

$$\begin{aligned} dt/d\tau &= \frac{E}{f(r)}, \\ (dr/d\tau)^2 &= E^2 - V, \\ d\phi/d\tau &= \frac{L}{r^2}, \end{aligned} \quad (3.1)$$

where $\{t, r, \theta, \phi\}$ are the usual Schwarzschild coordinates, the constants E and L are the energy and angular momentum per unit mass, respectively. The effective potential for radial motion is given by

$$V = f \left(1 + \frac{L^2}{r^2} \right). \quad (3.2)$$

To exploit the analogy with Keplerian orbits, it is useful to make the substitution

$$r(\chi) = \frac{pM}{1 + e \cos \chi}. \quad (3.3)$$

The parameter χ ranges from 0 to 2π as r goes from the periastron r_1 to the apastron r_2 and back to the periastron r_1 ; The constants p and e can be derived from E and L by letting $dr/d\tau = 0$ at the periastron and the apastron in Eq. (3.1), which leads to

$$\begin{aligned} E^2 &= E(p, e)^2 = \frac{(p-2-2e)(p-2+2e)}{p(p-3-e^2)}, \\ L^2 &= L(p, e)^2 = \frac{p^2 M^2}{p-3-e^2}. \end{aligned} \quad (3.4)$$

Integrating Eq. (3.1) gives [75]

$$\begin{aligned} t(\chi) &= p^2 M (p-2-2e)^{1/2} (p-2+2e)^{1/2} \\ &\times \int_0^\chi d\chi' (p-2-2e \cos \chi')^{-1} (1+e \cos \chi')^{-2} \\ &\times (p-6-2e \cos \chi')^{-1/2}, \end{aligned} \quad (3.5)$$

and

$$\phi(\chi) = p^{1/2} \int_0^\chi \frac{d\chi'}{(p-6-2e\cos\chi')^{1/2}}. \quad (3.6)$$

The radial period is given by $P = 2t(\pi)$. The radial frequency and the azimuthal frequency are given by $\Omega_r = 2\pi/P$ and $\Omega_\phi = \phi(2\pi)/P$, respectively. We now proceed with the calculation of the source term in Eqs. (2.12), taking the particle's worldline to be a bound geodesic in the Schwarzschild spacetime. After integration, the particle's stress-energy tensor becomes

$$\begin{aligned} T_p^{\alpha\beta}(x) &= m_p \frac{u^\alpha u^\beta}{r'^2 u^t} \delta(r-r') \delta(\cos\theta) \delta(\phi-\phi'), \\ S(x) &= \mu_s \frac{1}{r'^2 u^t} \delta(r-r') \delta(\cos\theta) \delta(\phi-\phi'). \end{aligned} \quad (3.7)$$

Here $\mu_s = 4\pi m_p d$ and $\{t, r', \pi/2, \phi'(t)\}$ describe the particle's worldline; the four-velocity $u^\alpha = dx'^\alpha/d\tau$ can be obtained from Eq. (3.1). Following the procedure given in [75] we get

$$\begin{aligned} S_{lm\omega}(r) &= \frac{\mu_s}{2\pi} {}_0Y_{lm}\left(\frac{\pi}{2}, 0\right) \int_{-\infty}^{+\infty} dt \frac{r' f}{r'^2 u^t} \delta(r-r') e^{i(\omega t - m\phi')} \\ &= \mu_s {}_0Y_{lm}\left(\frac{\pi}{2}, 0\right) P^{-1} \sum_k \delta(\omega - \omega_{mk}) \\ &\quad \times \int_0^P dt \frac{r' f}{r'^2 u^t} \delta(r-r') e^{i(\omega_{mk} t - m\phi')} \\ &= \mu_s {}_0Y_{lm}\left(\frac{\pi}{2}, 0\right) \Theta(r-r_1) \Theta(r_2-r) \\ &\quad \times f^2 P^{-1} (E^2 - V)^{-1/2} \sum_k \delta(\omega - \omega_{mk}) \\ &\quad \times \sum_{\pm} \frac{1}{r f} e^{\pm i[\omega_{mk} t(r) - m\phi(r)]}, \end{aligned} \quad (3.8)$$

where $\omega_{mk} = m\Omega_\phi + k\Omega_r$. Therefore, the solutions for scalar field at infinity and at the horizon are given by

$$\begin{aligned} X_{lm\omega}^{\infty, H}(r) &\sim \frac{e^{\pm i\omega r^*}}{2i\omega A_{lm\omega}^{\text{in}}} \int_{-\infty}^{+\infty} dr'^* X_{lm\omega}^{\text{in, up}}(r') S_{lm\omega}(r') \\ &\equiv \tilde{Z}_{lm\omega}^{\infty, H} e^{\pm i\omega r^*}. \end{aligned} \quad (3.9)$$

So we can get

$$\begin{aligned} \tilde{Z}_{lm\omega}^{\infty, H} &= \frac{1}{2i\omega A_{lm\omega}^{\text{in}}} \int_{-\infty}^{+\infty} dr'^* X_{lm\omega}^{\text{in, up}}(r') S_{lm\omega}(r') \\ &= \frac{\mu_s P^{-1}}{2i\omega A_{lm\omega}^{\text{in}}} {}_0Y_{lm}\left(\frac{\pi}{2}, 0\right) \sum_{\pm} \sum_k \delta(\omega - \omega_{mk}) \int_{r_1}^{r_2} dr \frac{X_{lm\omega}^{\text{in, up}}(r)}{r\sqrt{E^2 - V}} e^{\pm i[\omega_{mk} t(r) - m\phi(r)]} \\ &= \mu_s \sum_k Z_{lmk}^{\infty, H} \delta(\omega - \omega_{mk}). \end{aligned} \quad (3.10)$$

The formula for $dE_{\text{scal}}^{\infty,H}/dt$ and $dL_{\text{scal}}^{\infty,H}/dt$ caused by the scalar field at infinity and at the horizon are given by

$$\begin{aligned}\frac{dE_{\text{scal}}^{\infty,H}}{dt} &= \frac{\mu_s^2}{4\pi} \sum_{lmk} \omega_{mk}^2 |Z_{lmk}^{\infty,H}|^2 = 4\pi d^2 m_p^2 \sum_{lmk} \omega_{mk}^2 |Z_{lmk}^{\infty,H}|^2, \\ \frac{dL_{\text{scal}}^{\infty,H}}{dt} &= \frac{\mu_s^2}{4\pi} \sum_{lmk} m \omega_{mk} |Z_{lmk}^{\infty,H}|^2 = 4\pi d^2 m_p^2 \sum_{lmk} m \omega_{mk} |Z_{lmk}^{\infty,H}|^2.\end{aligned}\tag{3.11}$$

The formula for $dE_{\text{grav}}^{\infty,H}/dt$ and $dL_{\text{grav}}^{\infty,H}/dt$ caused by the tensor field are given in [75]. The total energy and angular momentum flux are

$$\begin{aligned}\dot{E}_{\text{tot}} &= \dot{E}_{\text{grav}} + \dot{E}_{\text{scal}} = \dot{E}_{\text{grav}}^{\infty} + \dot{E}_{\text{grav}}^H + \dot{E}_{\text{scal}}^{\infty} + \dot{E}_{\text{scal}}^H, \\ \dot{L}_{\text{tot}} &= \dot{L}_{\text{grav}} + \dot{L}_{\text{scal}} = \dot{L}_{\text{grav}}^{\infty} + \dot{L}_{\text{grav}}^H + \dot{L}_{\text{scal}}^{\infty} + \dot{L}_{\text{scal}}^H.\end{aligned}\tag{3.12}$$

Our method to calculate the bound orbital evolution of the Schwarzschild spacetime caused by radiation reaction is as follows. Based on the fact that the motion of the particle is geodesic over a time scale comparable to the orbital period, we adopt the adiabatic approximation in which the radiation reaction operates over a much longer time scale. The waves are generated by the orbiting particle, and the average is taken over several orbital periods. The orbital parameters change as follows

$$\left\langle \frac{dE_{\text{tot}}}{dt} \right\rangle = \dot{E}_{\text{tot}} = -m_p \dot{E}, \quad \left\langle \frac{dL_{\text{tot}}}{dt} \right\rangle = \dot{L}_{\text{tot}} = -m_p \dot{L}.\tag{3.13}$$

Using Eq. (3.13), we can then infer the time-averaged rates of change of the orbital parameters. Since E and L are functions of p and e , we have

$$\begin{aligned}-\dot{E}_{\text{tot}} &= m_p \frac{\partial E}{\partial p} \frac{dp}{dt} + m_p \frac{\partial E}{\partial e} \frac{de}{dt}, \\ -\dot{L}_{\text{tot}} &= m_p \frac{\partial L}{\partial p} \frac{dp}{dt} + m_p \frac{\partial L}{\partial e} \frac{de}{dt}.\end{aligned}\tag{3.14}$$

These equations can easily be inverted. Using Eqs. (3.4) and (3.14), we find

$$m_p \frac{dp}{dt} = \frac{2(p-3-e^2)^{1/2}}{(p-6-2e)(p-6+2e)} \left[p^{3/2}(p-2-2e)^{1/2}(p-2+2e)^{1/2} \dot{E}_{\text{tot}} - (p-4)^2 \dot{L}_{\text{tot}}/M \right]\tag{3.15}$$

and

$$m_p \frac{de}{dt} = \frac{(p-3-e^2)^{1/2}}{ep(p-6-2e)(p-6+2e)} \left[(1-e^2)(4e^2+(p-2)(p-6)) \dot{L}_{\text{tot}}/M - p^{3/2}(p-6-2e^2)(p-2-2e)^{1/2}(p-2+2e)^{1/2} \dot{E}_{\text{tot}} \right].\tag{3.16}$$

It is important to notice that Eqs. (3.15) and (3.16) are singular at $p = 6 + 2e$, where the trajectory stops.

The orbit-averaged trajectory is determined over time in terms of $\{p(t), e(t), \Phi_\varphi(t), \Phi_r(t)\}$. The phases $\Phi_{\varphi,r}$ given above are the integral over time of the orbit's fundamental frequencies:

$$\Phi_{\varphi,r} = \int_0^t dt' \Omega_{\varphi,r}(p(t'), e(t')). \quad (3.17)$$

EMRI waveforms are represented by the complex time-domain dimensionless strain

$$h_+ - ih_\times = -\frac{2m_p}{d_L} \sum_{lmk} \frac{Z_{\text{grav},lmk}^\infty}{\omega_{mk}^2} {}_{-2}Y_{lm}(\theta, 0) e^{im\phi} e^{-i\Phi_{mk}(t)}, \quad (3.18)$$

where $Z_{\text{grav},lmk}^\infty$ is the Teukolsky mode amplitude for tensor field Ψ_4 far away from the source [77], θ is the source-frame polar viewing angle, ϕ is the source-frame azimuthal viewing angle, d_L is the luminosity distance, and $\{l, m, k\}$ are the indices describing the frequency-domain harmonic mode decomposition. The indices l, m, k label the orbital angular momentum, azimuthal and radial modes, respectively. $\Phi_{mk}(t) = m\Phi_\varphi + k\Phi_r$ is the summation of decomposed phases for each given mode. To estimate the detectability of the scalar charge, we introduce the noise-weighted inner product to define the faithfulness between two templates

$$\langle s_1 | s_2 \rangle = 2 \int_{f_{\min}}^{f_{\max}} \frac{\tilde{s}_1(f) \tilde{s}_2^*(f) + \tilde{s}_1^*(f) \tilde{s}_2(f)}{S_n(f)} df, \quad (3.19)$$

$\tilde{s}_1(f)$ is the Fourier transform of the time domain signal, and its complex conjugate is $\tilde{s}_1^*(f)$. The faithfulness between two signals is defined as

$$\mathcal{F}[s_1, s_2] = \max_{\{t_c, \phi_c\}} \frac{\langle s_1 | s_2 \rangle}{\sqrt{\langle s_1 | s_1 \rangle \langle s_2 | s_2 \rangle}}, \quad (3.20)$$

where (t_c, ϕ_c) are time and phase offsets [81]. The signal and noise spectral density $S_n(f)$ for space-based detectors are given in [76, 77, 82].

4 Numerical results

As seen in Eq. (3.11), the numerical calculation of \dot{E}_{tot} and \dot{L}_{tot} involves the truncation of infinite sums over l and k . This truncation obviously limits the accuracy of the numerical results. We choose $l_{\max} = 6$, $k_{\min} = -4$ and $k_{\max} = 10$ to reach the accuracy about 10^{-4} for eccentric orbits with low eccentricities $e \leq 0.3$. In Table 1 we compare our results on the radiated energy and angular momentum flux with those in Refs. [75, 83] for two representative points in the $p - e$ plane. In order to efficiently interpolate the fluxes with bicubic splines, we introduce $y = \ln(p - p_s + 3.9)$ [84] and e to build a uniform grid in (y, e) space with $1.37 \leq y \leq 3.82$ and $0.0 \leq e \leq 0.3$ in steps of 0.025 where $p_s = 6 + 2e$ [85]. The large errors in the interpolation over the uniform grid of the actual flux values are intolerable. For the point $(p, e) = (6.688, 0.3)$, the actual energy and angular fluxes from the numerical calculation are 2.359×10^{-4} and 3.301×10^{-3} , the interpolated energy and angular momentum values are 2.450×10^{-4} and 3.377×10^{-3} , the relative errors can reach 3.83% and 2.31%. Generally we would like to control the relative error under $\sim 1\%$ [75]. In order to reduce the error in the interpolation, we subtract out the leading PN behavior from the actual

| (p, e) | (7.50478, 0.188917) | | (10, 0.2) | |
|--|--------------------------|--------------------------|--------------------------|--------------------------|
| | This paper | Ref [75] | This paper | Ref [83] |
| $M^2 \dot{E}_{\text{grav}}^\infty / m_p^2$ | 3.16698×10^{-4} | 3.16804×10^{-4} | / | / |
| $M^2 \dot{E}_{\text{grav}}^H / m_p^2$ | 4.54079×10^{-7} | / | / | / |
| $M^2 \dot{E}_{\text{scal}} / m_p^2$ | / | / | 3.21274×10^{-5} | 3.21331×10^{-5} |
| $M \dot{L}_{\text{grav}}^\infty / m_p^2$ | 5.96409×10^{-3} | 5.96562×10^{-3} | / | / |
| $M \dot{L}_{\text{grav}}^H / m_p^2$ | 7.62174×10^{-6} | / | / | / |
| $M \dot{L}_{\text{scal}} / m_p^2$ | / | / | 9.62487×10^{-4} | 9.62608×10^{-4} |

Table 1. Comparison of the results on the energy and angular momentum fluxes in this paper and those in Refs. [75, 83] for two representative points in the $p - e$ plane. For a given (p, e) , we calculate the energy \dot{E}_{scal} and angular momentum \dot{L}_{scal} carried away by the scalar field with the scalar charge $d = 1$, the energy $\dot{E}_{\text{grav}}^{\infty, H}$ and angular momentum $\dot{L}_{\text{grav}}^{\infty, H}$ carried away by the tensor field at infinity and at the horizon, respectively.

flux values and interpolate over the resulting effective fluxes $\dot{E}_{\text{spl}} = (\dot{E}_{\text{scal}} - \dot{E}_{\text{PN}})\Omega_\varphi^{-10/3}$ and $\dot{L}_{\text{spl}} = (\dot{L}_{\text{scal}} - \dot{L}_{\text{PN}})\Omega_\varphi^{-7/3}$. The leading PN behaviors for scalar fields are given by [59]

$$\begin{aligned}\dot{E}_{\text{PN}} &= \frac{1}{3} \frac{1 + e^2/2}{(1 - e^2)^{5/2}} \Omega_\varphi^{8/3}, \\ \dot{L}_{\text{PN}} &= \frac{1}{3} \frac{1}{1 - e^2} \Omega_\varphi^{5/3}.\end{aligned}\tag{4.1}$$

We construct bicubic splines over (y, e) of $(\dot{E}_{\text{spl}}, \dot{L}_{\text{spl}})$ and reconstruct the energy and angular momentum fluxes. For the same point $(p, e) = (6.688, 0.3)$, the interpolated energy and angular momentum flux values are 2.346×10^{-4} and 3.290×10^{-3} , the relative errors can reduce to 0.57% and 0.31%, which satisfies our accuracy goal. The effective fluxes $(\dot{E}_{\text{spl}}, \dot{L}_{\text{spl}})$ can be seen in Fig. 1. Making use of the FastEMRIWaveforms, based on the open code [77], we can add the influence of the scalar field into the code by adding scalar flux values and get fast trajectory evolution and waveforms.

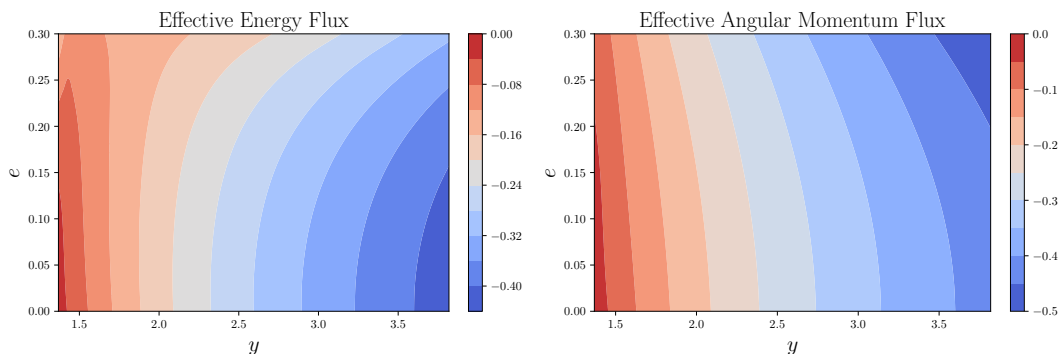


Figure 1. The effective energy flux and angular momentum flux for the scalar field with $d = 1$. The left panel shows the effective energy flux \dot{E}_{spl} and the right panel shows the effective angular momentum flux \dot{L}_{spl} .

We choose EMRI systems with $M = 10^6 M_\odot$ for the central BH and $m_p = 10 M_\odot$ for the small BH. The orbital evolution from different initial conditions with various scalar charges

is shown in Fig. 2. We find that the orbital parameter p always decreases with time and the rate of change is faster for larger scalar charge d . Scalar fields accelerate the evolution of p since the scalar fields carry away additional energy and angular momentum to make the particle fall into the central BH faster. For the orbital parameter e , the eccentricity decreases first and then increases near $p_s = 6 + 2e$. This change of eccentricity e can be interpreted as a precursor effect to the eventual plunging of the orbit caused by the strong field effect, as discussed in [75]. Furthermore, we find that the time it takes e to reach the minimum is shorter and the values of p and e at the turning point when e reaches the minimum are bigger for larger scalar charge d . The reason is that both the scalar and tensor fields enhance the gravitational field so that the strong field effect comes into play further away from the central BH. It's obvious from Eq. (3.11) that the scalar field with a bigger scalar charge d carries away more energy and angular momentum to make the evolution of parameters faster. Given a scalar charge, we can quantify the GR deviation caused by the scalar field with the scalar charge through the number of cycles accumulated after long-time evolution. Fig. 3 shows the accumulated dephasing $\Delta\Phi = \Phi_\varphi(d) - \Phi_\varphi(d=0)$ with time for different initial values of p_0 and e_0 . Fig. 4 shows the accumulated dephasing $\Delta\Phi = \Phi_\varphi(d) - \Phi_\varphi(d=0)$ with time for different initial values of r_a and e_0 as discussed in [76], here $r_a = p_0/(1 - e_0)$ is the apastron. Starting from a smaller orbital distance with $p_0 \leq 8$, the accumulated dephasing $\Delta\Phi$ is bigger for larger initial eccentricity e_0 for the same evolution time. However, starting from a larger orbital distance with $p \geq 20$, the accumulated dephasing $\Delta\Phi$ is smaller for larger initial eccentricity e_0 for the same evolution time. If we use different initial values of the apastron r_a , then we find that the accumulated dephasing $\Delta\Phi$ is always bigger for larger initial eccentricity e_0 regardless of the initial values of r_a . This result shows different behaviors between weak and strong fields for eccentric orbits and we will explain it in the next section. In Fig. 5 we show the dephasing $\Delta\Phi$ as a function of the scalar charge d for EMRIs with different eccentricities and different masses for the central BH. The results show that bigger values of the scalar charge lead to larger dephasing, and the dephasing decreases with a larger mass for the central BH and a larger initial eccentricity.

It's obvious that larger $\Delta\Phi$ helps LISA detect the scalar charge easier for quasicircular orbits. However, for eccentric orbits the ability of distinguishing modified gravity from GR not only depends on $\Delta\Phi$ but also depends on the eccentricity e . For the convenience of discussion, we assume that starting at $t = 0$ the initial phase and positions of the small BH are the same for the situation with and without scalar charges. Fig. 6 shows the GW waveforms with the scalar charge $d = 0.002$ and $d = 0$ after a long-time evolution from the initial position. We see that as $\Delta\Phi$ accumulates, the dephasing between the waveforms becomes apparent at the time $t = 10714950$ s. The amplitude shapes of GWs are different for different eccentricities and the waveforms become sharper for higher eccentricities. It was argued in Ref. [86] that two signals can be distinguished by LISA if $\mathcal{F}_n \leq 0.988$. In Figs. 7 and 8, we show the faithfulness between two GW signals with and without the scalar charge as a function of the scalar charge d for different eccentric orbits. These results suggest that LISA can detect the scalar charge around $d \geq 0.005$ through one-year observation of EMRIs consisting of a central BH with the mass $M = 10^6 M_\odot$ and a small BH with the mass $m_p = 10 M_\odot$. For EMRIs with $M = 5 \times 10^6 M_\odot$ and $m_p = 10 M_\odot$, the detection limit for the scalar charge with LISA is $d \geq 0.02$. From Figs. 7 and 8, we see that the effect of the scalar charge is more significant for eccentric inspirals than circular inspirals, d is correlated with M and is anti-correlated with e_0 .

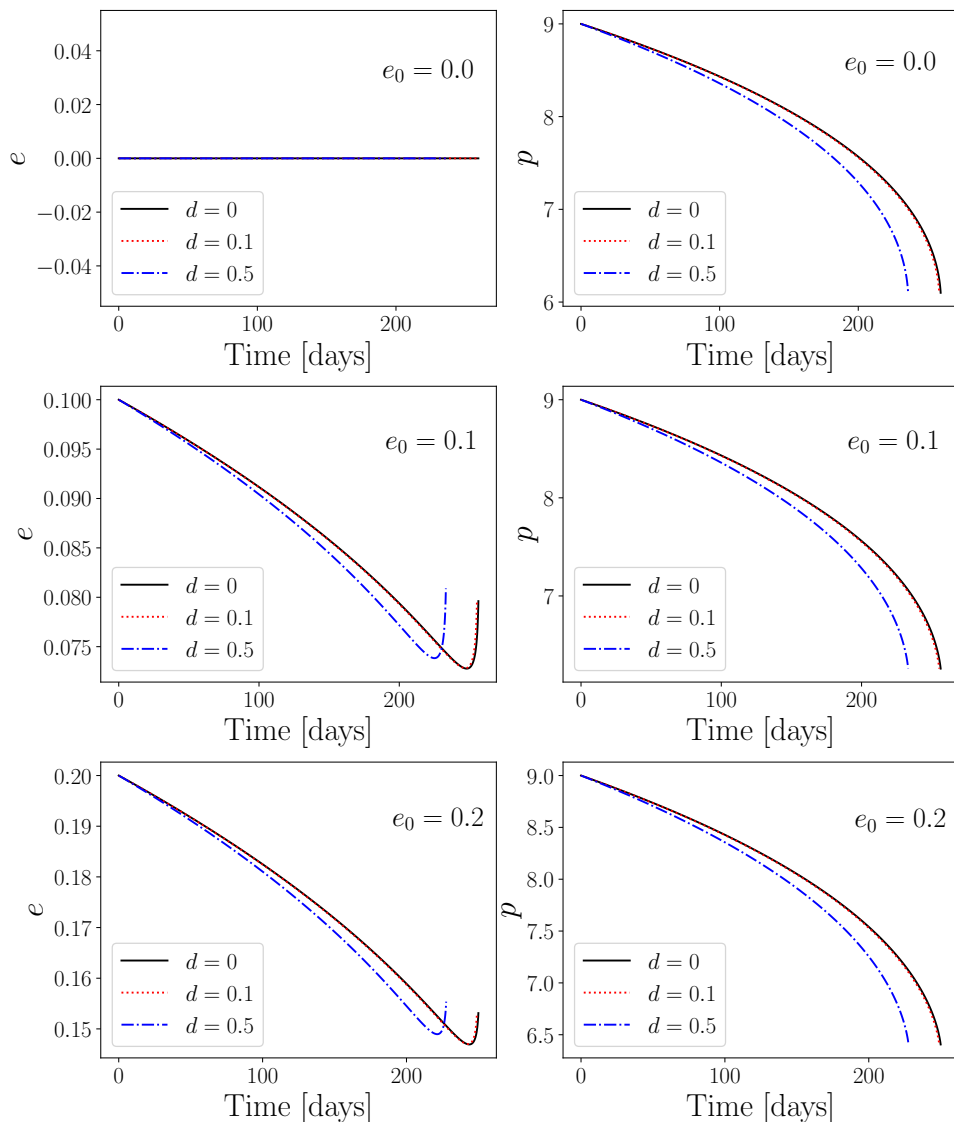


Figure 2. The orbital evolution for different values of the scalar charge. The initial conditions are chosen as $(p_0, e_0) = (9.0, 0.0)$, $(9.0, 0.1)$ and $(9.0, 0.2)$, respectively. The left panels show the evolution of the eccentricity e with time, and the right panels show the evolution of p with time.

5 Analytical results

In order to understand the strange behaviors of $\Delta\Phi$ for eccentric orbits with different initial values of p_0 and e_0 as shown in Fig. 3 and the numerical results presented in Ref. [76], we calculate both scalar and gravitational energy fluxes emitted to infinity for eccentric orbits. We expand the ingoing wave function $X_{\omega lm}^{\text{in}}$ in terms of small parameters $z = \omega r \sim v$ and $\epsilon = 2M\omega \sim v^3$ [87],

$$X_{\omega 0m}^{\text{in}} = z - \frac{z^3}{6} + \epsilon \left(\frac{-5z^2}{6} + \frac{17z^4}{180} \right),$$

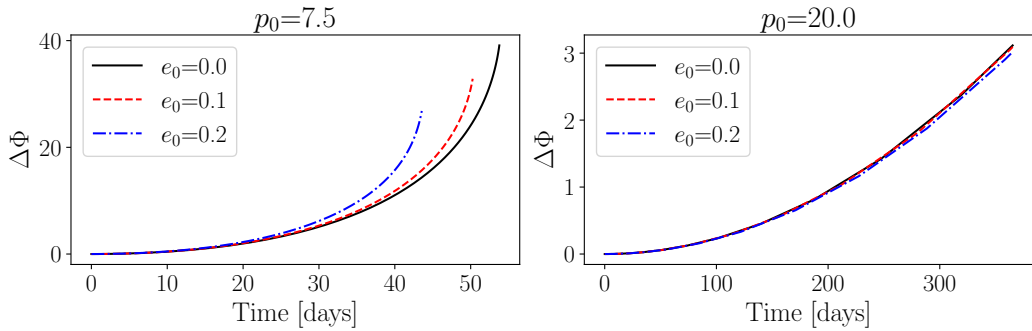


Figure 3. The accumulated orbital phase difference $\Delta\Phi = \Phi_\varphi(d = 0.1) - \Phi_\varphi(d = 0)$ as a function of time for different eccentric orbits. The initial values of the semi-latus rectum are $p_0 = 7.5$ and $p_0 = 20$ in the left and right panels, respectively.

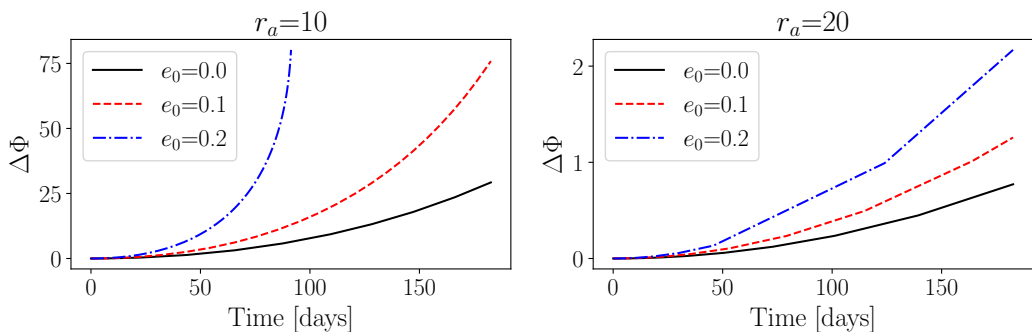


Figure 4. The accumulated orbital phase difference $\Delta\Phi = \Phi_\varphi(d = 0.1) - \Phi_\varphi(d = 0)$ as a function of time for different eccentric orbits. The initial values of the apastron are $r_a = 10$ and $r_a = 20$ in the left and right panels, respectively.

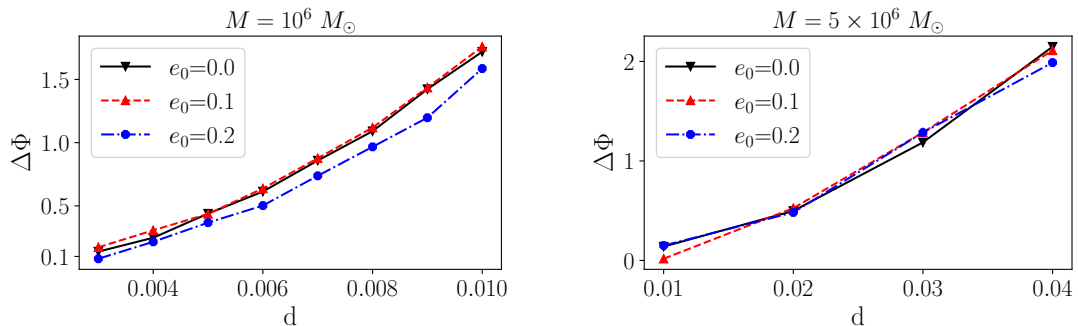


Figure 5. The accumulated orbital phase difference $\Delta\Phi = |\Phi_\varphi(d) - \Phi_\varphi(d = 0)|$ versus the scalar charge for different initial values of the eccentricity e_0 and different masses for the central BH of EMRIs. e_0 is the initial eccentricity that inspiral starts and p_0 is adjusted to ensure one-year observation before the merger. The left panel represents the EMRIs with $M = 10^6 M_\odot$ and $m_p = 10 M_\odot$ and the right panel represents the EMRIs with $M = 5 \times 10^6 M_\odot$ and $m_p = 10 M_\odot$.

$$X_{\omega 1m}^{\text{in}} = \frac{z^2}{3} - \frac{z^4}{30} + \frac{z^6}{840} + \epsilon \left(\frac{-z}{6} - \frac{-7z^3}{60} + \frac{151z^5}{15120} \right),$$

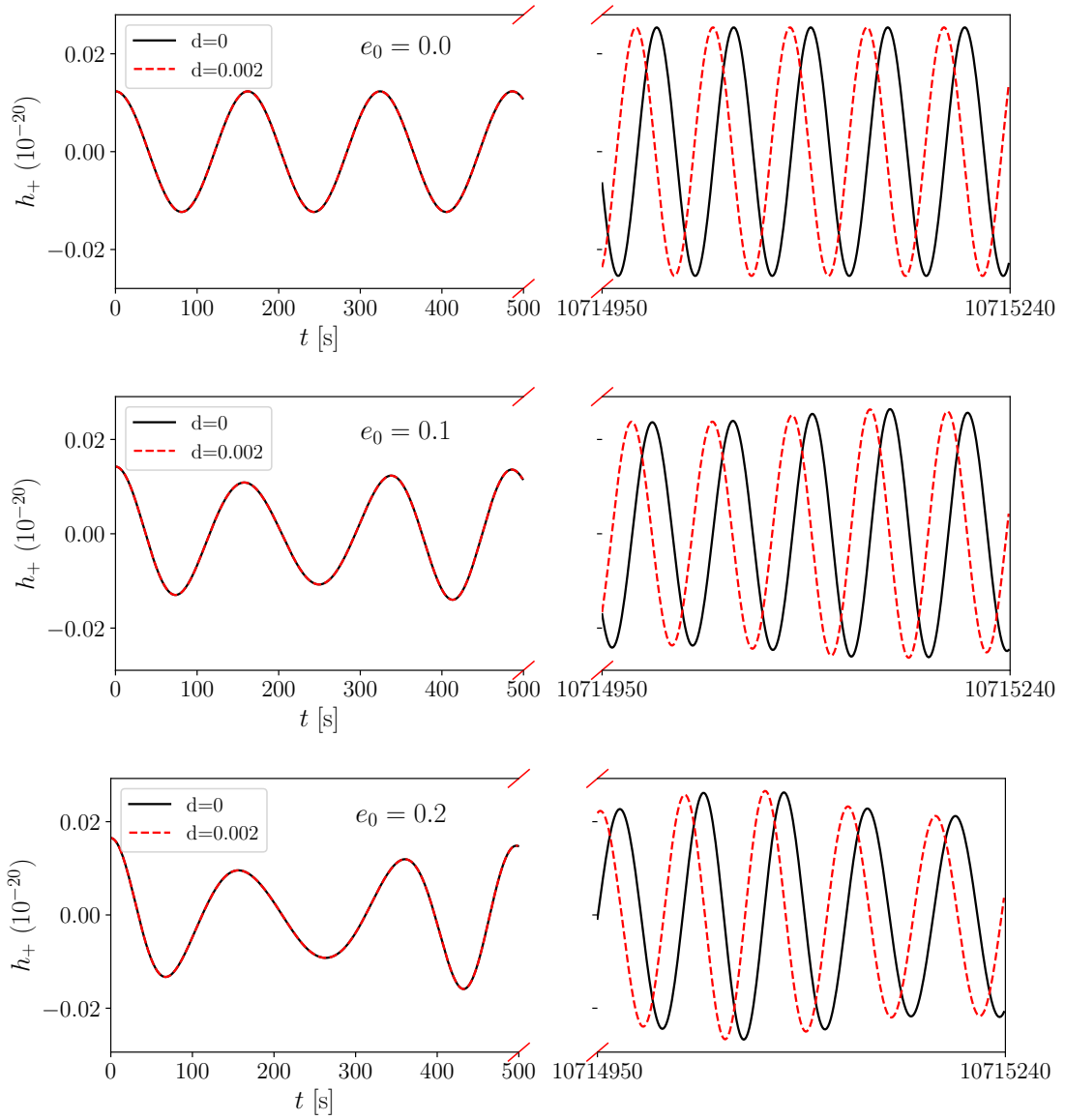


Figure 6. The waveforms with different scalar charge d for different initial values of the eccentricity e_0 after a long-time evolution. Here we take the initial semi-latus rectum $p_0 = 14$, and the luminosity distance $d_L = 1$ Gpc.

$$\begin{aligned}
 X_{\omega 2m}^{\text{in}} &= \frac{z^3}{15} - \frac{z^5}{210} + \epsilon \left(\frac{-z^2}{15} - \frac{4z^4}{315} + \frac{z^6}{1080} \right), \\
 X_{\omega 3m}^{\text{in}} &= \frac{z^4}{105}.
 \end{aligned} \tag{5.1}$$

For $A_{lm\omega}^{\text{in}}$, we obtain [87]

$$A_{lm\omega}^{\text{in}} = \frac{1}{2} i^{l+1} e^{-i\epsilon \ln \epsilon} \left[1 + \epsilon \left(p_{lm}^{(1)} + i q_{lm}^{(1)} \right) + \dots \right], \tag{5.2}$$

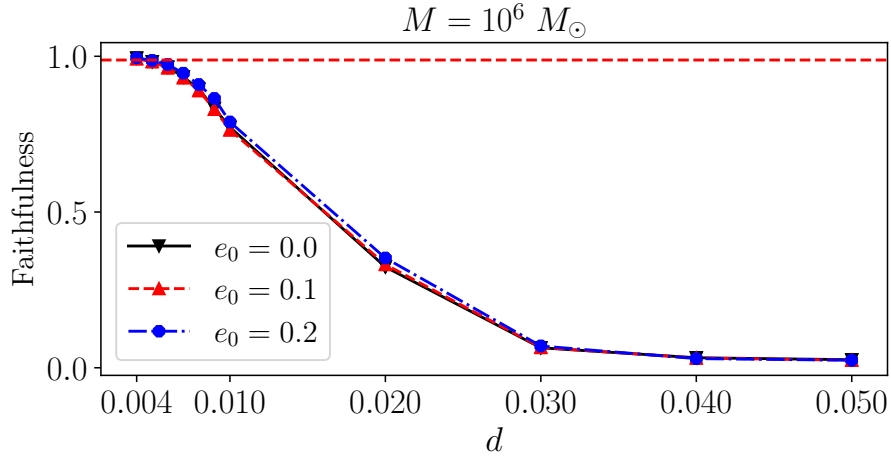


Figure 7. The faithfulness of GW signals between the case with and without the scalar charge as a function of the scalar charge d when $M = 10^6 M_\odot$. e_0 is the initial eccentricity that inspiral starts, and p_0 is adjusted to ensure one-year observation before the merger. The horizontal dashed line represents the detection limit $\mathcal{F}_n \leq 0.988$ with LISA.

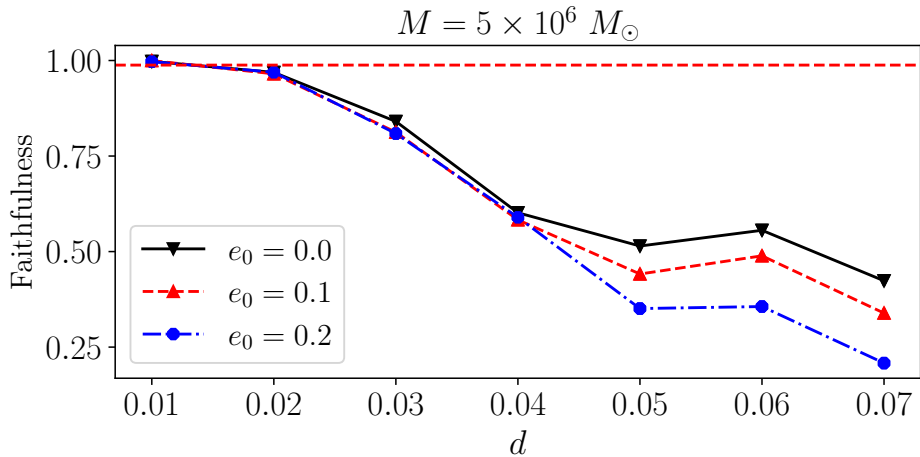


Figure 8. The faithfulness of GW signals between the case with and without the scalar charge as a function of the scalar charge d when $M = 5 \times 10^6 M_\odot$. e_0 is the initial eccentricity that inspiral starts, and p_0 is adjusted to ensure one-year observation before the merger. The horizontal dashed line represents the detection limit $\mathcal{F}_n \leq 0.988$ with LISA.

where

$$\begin{aligned}
 p_{lm}^{(1)} &= -\frac{\pi}{2}, \\
 q_{lm}^{(1)} &= \frac{1}{2} [\psi(l) + \psi(l+1) - 1] + \frac{2l+1}{2l} - \ln 2, \\
 \psi(l) &= \sum_{k=1}^{l-1} \frac{1}{k} - \gamma,
 \end{aligned} \tag{5.3}$$

and γ is the Euler constant. Geodesic orbits in Schwarzschild spacetime can be specified with two orbital elements, the semi-latus rectum p and the eccentricity e . We consider the expansion of quantities in terms of small parameters, $v = \sqrt{1/p}$ and e . For the radial frequency in geodesic equations, the expansion up to $\mathcal{O}(e^2, v^7)$ is

$$\Omega_r = \left(1 - \frac{3e^2}{2}\right)v^3 + \left(-3 + \frac{15e^2}{2}\right)v^5 + \left(-\frac{9}{2} + 6e^2\right)v^7. \quad (5.4)$$

The total scalar luminosity up to $\mathcal{O}(v^5)$ is,

$$\begin{aligned} \frac{dE_{\text{scal}}^\infty}{dt} = & \left(\frac{dE}{dt}\right)_D \left\{ 1 - 2v^2 + 2\pi v^3 - 10v^4 + \frac{12\pi v^5}{5} \right. \\ & \left. + e^2 \left(-1 + \frac{158v^2}{15} + 3\pi v^3 - \frac{4268v^4}{105} + \frac{47\pi v^5}{3} \right) \right\}, \end{aligned} \quad (5.5)$$

where

$$\left(\frac{dE}{dt}\right)_D = \frac{d^2}{3} \left(\frac{m_p}{M}\right)^2 v^8. \quad (5.6)$$

From Eq. (5.5), we see that when the secondary compact object is in the weak field regions ($p > 20$), $v \ll 1$, the e^2 term is negative, so binaries in more eccentric orbits emit less energy through the scalar field, and the orbital phase difference $\Delta\Phi$ is smaller. When the secondary compact object is in relative strong field regions ($p < 8$), $v \sim 1$, the e^2 term becomes positive, so binaries in more eccentric orbits emit more energy, and the orbital phase difference $\Delta\Phi$ is larger. If we replace the semi-latus rectum p with the apastron r_a , then Eq. (5.5) can be rewritten

$$\begin{aligned} \frac{dE_{\text{scal}}^\infty}{dt} = & \frac{d^2}{3} \left(\frac{m_p}{M}\right)^2 \frac{1}{r_a^4} \left\{ 1 - \frac{2}{r_a} + \frac{2\pi}{r_a^{3/2}} - \frac{10}{r_a^2} + \frac{12\pi}{5r_a^{5/2}} \right. \\ & \left. + e \left(4 - \frac{10}{r_a} + \frac{11\pi}{r_a^{3/2}} - \frac{60}{r_a^2} + \frac{78\pi}{5r_a^{5/2}} \right) \right\}. \end{aligned} \quad (5.7)$$

The e term is always positive, so the orbital phase difference $\Delta\Phi$ is always larger in more eccentric orbits. The monopolar contribution of the scalar sector is

$$\frac{dE_{l=0, m=0}^\infty}{dt} = \left(\frac{dE}{dt}\right)_D \left(\frac{25v^2}{6} - \frac{35v^4}{2} + \frac{25}{3}\pi v^5 \right) e^2. \quad (5.8)$$

So the monopole radiation only appears for eccentric binaries and the contribution to the luminosity is in the order of $d^2 e^2 v^{10}$. The dipolar contribution of the scalar sector is

$$\begin{aligned} \frac{dE_{l=1, m=1}^\infty}{dt} = & \left(\frac{dE}{dt}\right)_D \left\{ 1 - \frac{26v^2}{5} + 2\pi v^3 + \frac{1123v^4}{175} - \frac{52}{5}\pi v^5 \right. \\ & \left. + e^2 \left(-1 + \frac{19v^2}{10} + 3\pi v^3 + \frac{8496v^4}{175} - \frac{321}{5}\pi v^5 \right) \right\}. \end{aligned} \quad (5.9)$$

In the weak field regions, the dipolar contribution to the luminosity is in the order of $d^2 v^8$ and the eccentricity reduces the contribution. The quadrupolar contribution of the scalar

sector is

$$\begin{aligned} \frac{dE_{l=2,m=2}^{\infty}}{dt} = & \left(\frac{dE}{dt} \right)_D \left\{ \frac{16v^2}{5} - \frac{848v^4}{35} + \frac{64\pi v^5}{5} \right. \\ & \left. + e^2 \left(\frac{67v^2}{15} - \frac{4481v^4}{42} + \frac{1073\pi v^5}{15} \right) \right\}. \end{aligned} \quad (5.10)$$

In the weak field regions, the quadrupolar contribution to the luminosity is in the order of d^2v^{10} and the eccentricity increases the contribution. Therefore, the monopolar contribution is negligible and the major contribution is from the dipolar radiation for the scalar sector in the weak field regions. The gravitational luminosity of the tensor sector is [88],

$$\begin{aligned} \frac{dE_{\text{grav}}^{\infty}}{dt} = & \left(\frac{dE}{dt} \right)_N \left\{ 1 - \frac{1247}{336}v^2 + 4\pi v^3 - \frac{44711}{9072}v^4 - \frac{8191\pi}{672}v^5 \right. \\ & \left. + e^2 \left(\frac{37}{24} - \frac{65v^2}{21} + \frac{1087\pi v^3}{48} - \frac{474409v^4}{9072} - \frac{118607\pi v^5}{1344} \right) \right\}, \end{aligned} \quad (5.11)$$

where

$$\left(\frac{dE}{dt} \right)_N = \frac{32}{5} \left(\frac{m_p}{M} \right)^2 v^{10}. \quad (5.12)$$

In the weak field regions, the total gravitational luminosity is in the order of v^{10} , so the ratio between the scalar and gravitational energy fluxes is in the order of d^2/v^2 . As the secondary compact object moves closer to the center massive BH, the ratio becomes smaller.

6 Parameter estimation

To consider degeneracies among the source parameters and give a more accurate analysis on the detectability of the scalar charge with LISA, we carry out the parameter estimation with the FIM method. In the time domain, the GW signal is mainly determined by parameters

$$\xi = (\ln M, \ln m_p, p_0, e_0, d, \theta_s, \phi_s, \theta_1, \phi_1, d_L). \quad (6.1)$$

In the large SNR limit, the covariances of source parameters ξ are given by the inverse of the Fisher information matrix

$$\Gamma_{ij} = \left\langle \frac{\partial h}{\partial \xi_i} \middle| \frac{\partial h}{\partial \xi_j} \right\rangle_{\xi=\xi}. \quad (6.2)$$

The statistical error on ξ and the correlation coefficients between the parameters are provided by the diagonal and non-diagonal parts of $\Sigma = \Gamma^{-1}$, i.e.

$$\sigma_i = \Sigma_{ii}^{1/2}, \quad c_{\xi_i \xi_j} = \Sigma_{ij} / (\sigma_{\xi_i} \sigma_{\xi_j}). \quad (6.3)$$

Because of the triangle configuration of the space-based GW detector regarded as a network of two L-shaped detectors, with the second interferometer rotated of 60° with respect to the first one, the total SNR can be written as the sum of SNRs of two L-shaped detectors [75]

$$\rho = \sqrt{\rho_1^2 + \rho_2^2} = \sqrt{\langle h_1 | h_1 \rangle + \langle h_2 | h_2 \rangle}, \quad (6.4)$$

where h_1 and h_2 denote the signals detected by two L-shaped detectors. The total covariance matrix of the source parameters is obtained by inverting the sum of the Fisher matrices

$\sigma_{\xi_i}^2 = (\Gamma_1 + \Gamma_2)_{ii}^{-1}$. Here we fix the source angles $\theta_s = \pi/3$, $\phi_s = \pi/2$, the direction of angular momentum $\theta_1 = \pi/4$, $\phi_1 = \pi/4$, and the initial orbital separation is adjusted to experience one-year adiabatic evolution before the final plunge $r_{\text{end}} = r_{\text{ISCO}} + 0.1 M$. As mentioned above, we consider the EMRI system with $m_p = 10 M_\odot$, $M = 10^6 M_\odot$, $d = 0.05$, $d_L = 1$ Gpc and $e_0 = (0.01, 0.1, 0.2, 0.29)$. By adding the scalar flux (3.12) into the FastEMRIWaveforms, we use the SchAAK module to get the signals in LISA. SNR for LISA is about ~ 46 with the one-year observation of eccentric EMRIs. Taking only the intrinsic parameters $\xi = (M, \mu, p_0, e_0, d)$, we obtain the error $\sigma_d = 4.0 \times 10^{-3}$ for $e_0 = 0.29$; $\sigma_d = 3.4 \times 10^{-3}$ for $e_0 = 0.2$; $\sigma_d = 4.5 \times 10^{-3}$ for $e_0 = 0.1$; and $\sigma_d = 6.7 \times 10^{-3}$ for $e_0 = 0.01$. As shown in Fig. 9, the eccentricity helps to reduce the measurement error of the scalar charge and improve the detectability of scalar fields. Comparing the errors of the scalar charge for $e_0 = 0.2$ and $e_0 = 0.29$, we find that the error of the scalar charge is larger when the initial eccentricity is $e_0 = 0.29$. When $e_0 = 0.29$, the dephasing between EMRIs with and without scalar charge is smaller, and the dephasing becomes the major factor on the detection of the scalar charge compared with the influence on the amplitude shapes of GWs caused by eccentricity, thus the estimation error of the scalar charge is larger. The corner plot of the parameters for $e_0 = 0.2$ is shown in Fig. 10. The results show that the relative measurement error of the scalar charge d is less than 10%, d is highly correlated with the mass of the Schwarzschild BH and is anti-correlated with the mass of the small compact object and the initial eccentricity. The anti-correlation between d and e_0 is consistent with the results shown in Fig. 9. The FIM results on the correlation between d and M and the anti-correlation between d and e_0 are consistent with the faithfulness analyses shown in Figs. 7 and 8. In order to constrain the scalar charge, we give the relative error of the scalar charge as a function of the scalar charge with SNR= 46 and SNR= 150 in Fig. 11. The results show that LISA could detect the scalar charge as small as $d \sim 0.014$ by excluding $d = 0$ at the 3σ confidence level with one-year observation of eccentric EMRIs with SNR=150, and $d \sim 0.023$ with SNR=46.

7 Conclusions

In modified gravity, BHs may carry scalar charge. In this paper, we consider the detection of scalar charge carried by the secondary BH in EMRIs as a probe of modified gravity. We derive the source term $S_{lm\omega}$ of the inhomogeneous Teukolsky equation for the scalar field in eccentric orbits, and calculate the energy and angular momentum emitted by the scalar field. In order to reduce the numerical error, we subtract out the leading PN behavior from the actual flux values and interpolate over an effective flux. We find that scalar fields accelerate the evolution of p due to the additional energy and angular momentum carried away by the scalar fields. For the orbital parameter e , the eccentricity decreases first and then increases near $p_s = 6 + 2e$. The time that it takes e to reach the minimum is shorter and the values of p and e at the turning point are bigger for larger scalar charge d .

Starting from relative strong field regions with smaller orbital distance ($p_0 \leq 8$), the contribution from the eccentricity is positive, so binaries in more eccentric orbits emit more energy, and the accumulated dephasing $\Delta\Phi$ is bigger for larger initial eccentricity e_0 . However, starting from weak field regions with larger orbital distance ($p \geq 20$), the contribution from the eccentricity is negative, so binaries in more eccentric orbits emit less energy through the scalar field, and the accumulated dephasing $\Delta\Phi$ is smaller for larger initial eccentricity e_0 . If instead we use the apastron r_a as the orbital distance, then the contribution from the

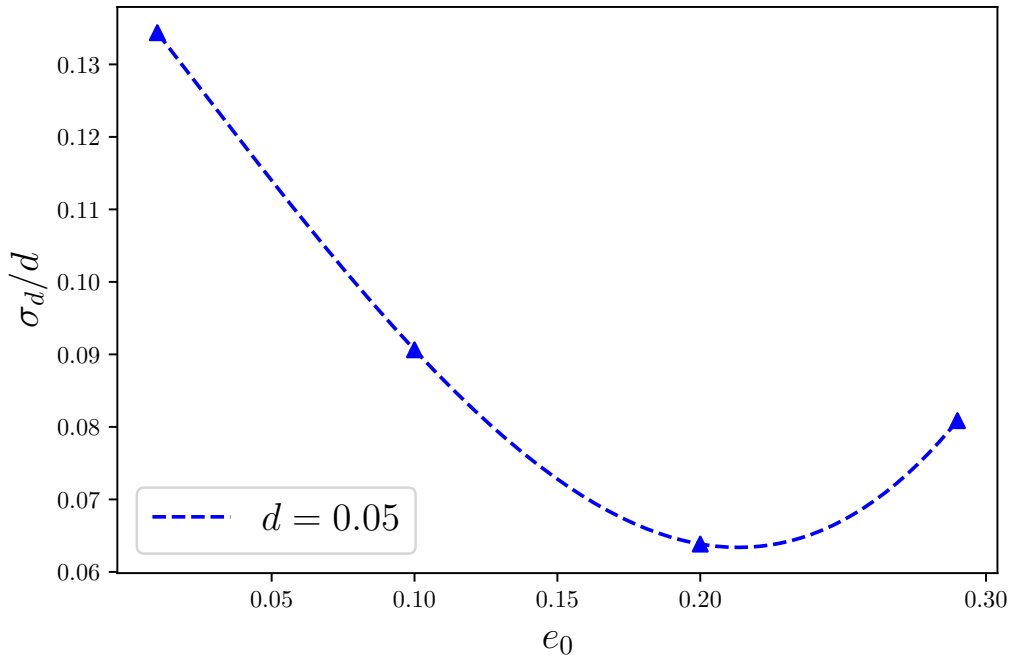


Figure 9. The relative 1 – σ error of the scalar charge d from the one-year observation of EMRIs with $d = 0.05$ and different initial eccentricity e_0 for LISA.

eccentricity is always positive, and the accumulated dephasing $\Delta\Phi$ is always bigger for larger initial eccentricity e_0 regardless of the initial values of r_a .

We find that the effect of the scalar charge is more significant for eccentric inspirals than circular inspirals and the mass of the central BH affects the detection of the scalar charge. For more massive central BHs, for example $M = 5 \times 10^6 M_\odot$, if the frequency of the higher harmonic is in LISA’s sensitive frequency band, the effect of the eccentricity is likely more significant and improves the detectability of the scalar charge. By computing the faithfulness between two signals with and without the scalar charge, we conclude that LISA can detect the scalar charge around $d \geq 0.005$ through one-year observation of EMRIs consisting of a central BH with the mass $M = 10^6 M_\odot$ and a small BH with the mass $m_p = 10 M_\odot$. For EMRIs with $M = 5 \times 10^6 M_\odot$ and $m_p = 10 M_\odot$, the detection limit for the scalar charge with LISA is $d \geq 0.02$. By estimating the measurement error of the scalar charge with the FIM method for EMRIs with $M = 10^6 M_\odot$ and $m_p = 10 M_\odot$, we find that LISA could detect the scalar charge as small as $d \sim 0.014$ by excluding $d = 0$ at the 3σ confidence level with one-year observation of eccentric EMRIs with SNR=150 and $d \sim 0.023$ with SNR=46, d is highly correlated with the mass M of the Schwarzschild BH and is anti-correlated with the mass m_p of the small compact object and the initial eccentricity. The FIM results confirmed the results obtained with faithfulness, and tell us that eccentric orbits can help us detect scalar fields. The correlation between d and M is consistent with the result found in [13] for circular EMRIs with Schwarzschild black hole, but the correlation between d and M and the anti-correlation between d and m_p are opposite to those found for eccentric EMRIs with the Kerr BH in Ref. [14]. This may be due to the effect of the spin of the Kerr BH in the Appendix A and the reason will be studied in future work.

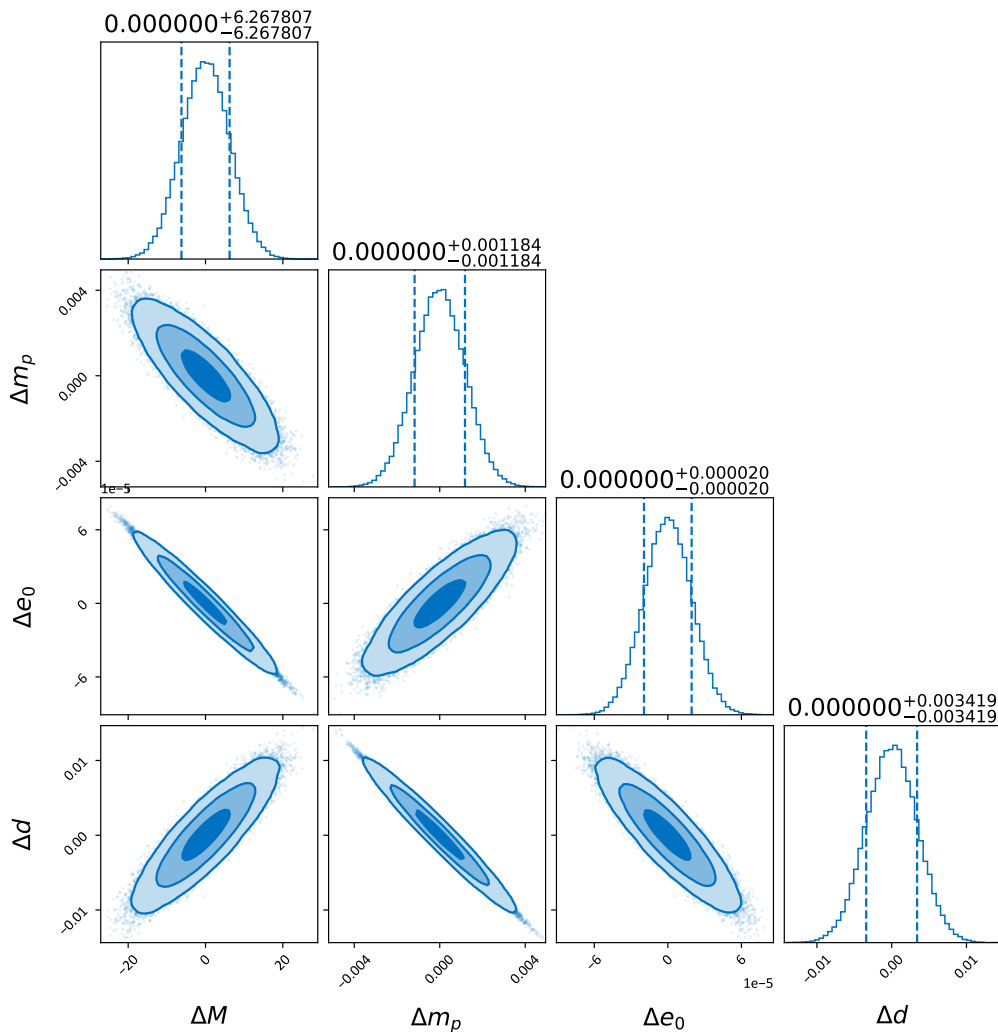


Figure 10. The corner plot for the probability distribution of the masses, the semi-latus rectum, eccentricity and electric charge, (M, m_p, e_0, d) , inferred from one-year observation of EMRIs with $d = 0.05$ and $e_0 = 0.2$ for LISA. Vertical lines show the $1 - \sigma$ interval for each source parameter. The contours correspond to 68%, 95% and 99% probability confidence intervals.

Acknowledgments

This work makes use of the Black Hole Perturbation Toolkit package. The numerical computations were performed at the public computing service platform provided by Network and Computing Center of HUST. This research is supported in part by the National Key Research and Development Program of China under Grant No. 2020YFC2201504, the National Natural Science Foundation of China under Grant Nos. 11875136 and 12147120, and China Postdoctoral Science Foundation under Grant No. 2021TQ0018.

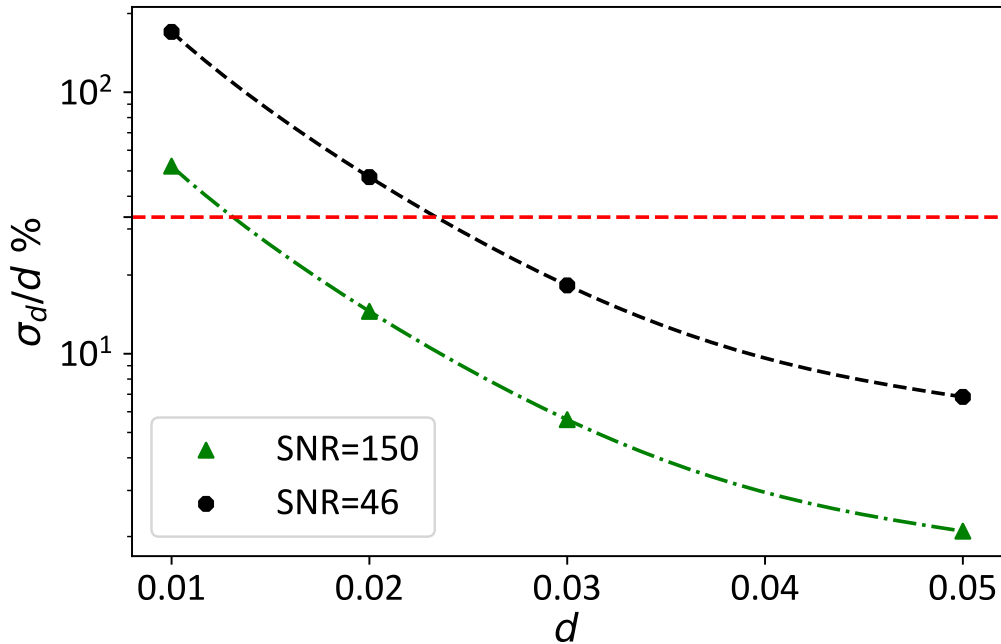


Figure 11. The relative error of the scalar charge d as a function of scalar charge from the one-year observation of EMRIs with eccentricity $e_0 = 0.2$ for LISA. The horizontal dashed line represents $3 - \sigma$ limit and its value is 33.3%.

A Comparison of Fisher information matrix of the Schwarchild case and Kerr case

We consider EMRIs with a scalar charged compact object inspiralling onto a Kerr BH and a Schwarchild BH in quasi-circular orbits. Following the procedure [14], we give the corner plot for the probability distribution of the masses, primary spin, and secondary charge, (M, m_p, a, d) , inferred after one year of observation with LISA for and EMRI with $d = 0.05$ and SNR of 150 in Fig. 12. Off-diagonal panels show that the scalar charge is highly correlated with the secondary mass and anti-correlated with the spin parameter and the mass of the primary, which are consistent with the results in [14]. We also compare the corner plot for charged EMRIs in the Schwarchild BH background in Fig. 13. The reason is that the spin parameter is associated with parameters such as scalar charge, secondary mass, primary mass, and other parameters. So including the primary spin parameter may influence the relation between d and m_p , d and M .

References

- [1] LIGO SCIENTIFIC AND VIRGO collaboration, Observation of Gravitational Waves from a Binary Black Hole Merger, *Phys. Rev. Lett.* **116** (2016) 061102 [1602.03837].
- [2] LIGO SCIENTIFIC, VIRGO collaboration, *GW150914: The Advanced LIGO Detectors in the Era of First Discoveries*, *Phys. Rev. Lett.* **116** (2016) 131103 [1602.03838].

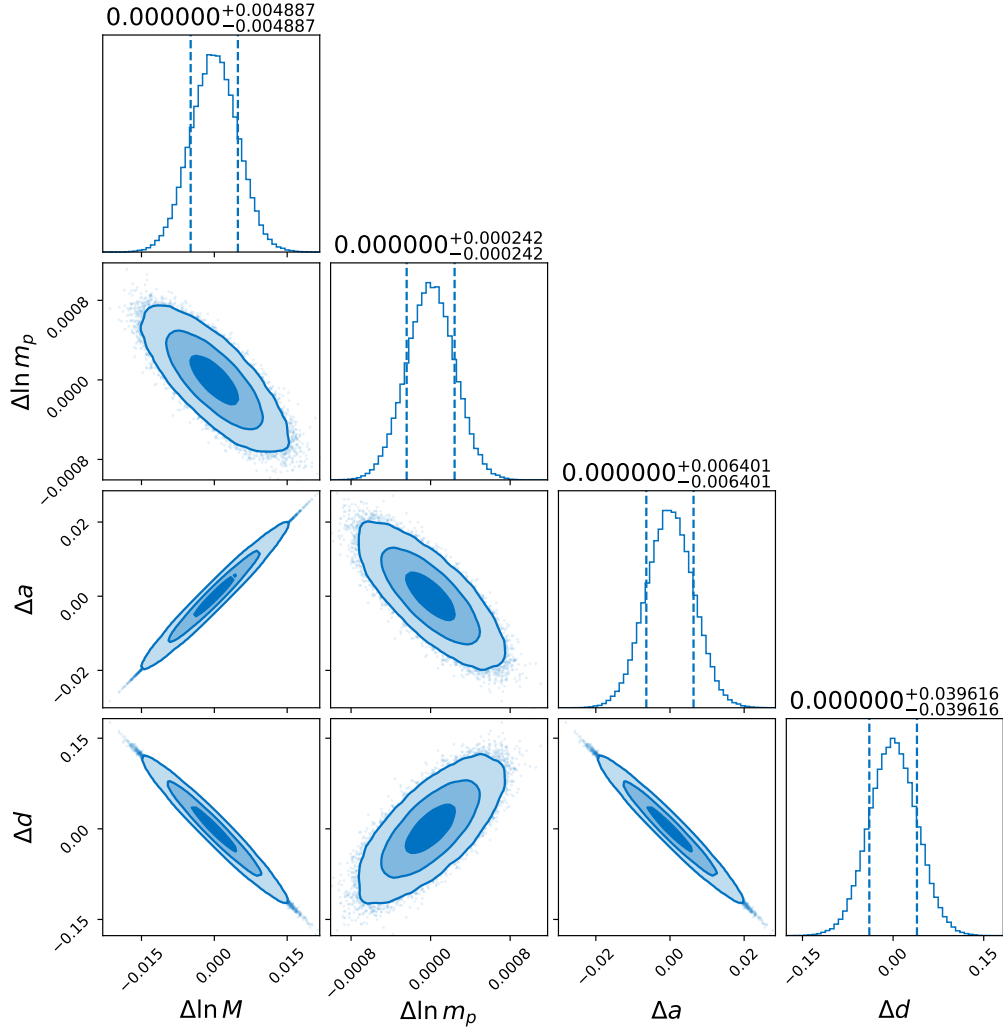


Figure 12. Corner plot for the probability distribution of the source parameters ($\ln M, \ln m_p, a, d$) with LISA, inferred after one-year observations of EMRIs with $d = 0.05$ and $a = 0$. Vertical lines show the 1σ interval for the source parameter. The contours correspond to the 68%, 95%, and 99% probability confidence intervals.

- [3] LIGO SCIENTIFIC, VIRGO collaboration, *GWTC-1: A Gravitational-Wave Transient Catalog of Compact Binary Mergers Observed by LIGO and Virgo during the First and Second Observing Runs*, *Phys. Rev. X* **9** (2019) 031040 [[1811.12907](#)].
- [4] LIGO SCIENTIFIC, VIRGO collaboration, *GWTC-2: Compact Binary Coalescences Observed by LIGO and Virgo During the First Half of the Third Observing Run*, *Phys. Rev. X* **11** (2021) 021053 [[2010.14527](#)].
- [5] LIGO SCIENTIFIC, VIRGO collaboration, *GWTC-2.1: Deep Extended Catalog of Compact Binary Coalescences Observed by LIGO and Virgo During the First Half of the Third Observing Run*, [2108.01045](#).
- [6] LIGO SCIENTIFIC, VIRGO, KAGRA collaboration, *GWTC-3: Compact Binary Coalescences Observed by LIGO and Virgo During the Second Part of the Third Observing Run*, [2111.03606](#).
- [7] J. Kormendy and D. Richstone, *Inward bound: The Search for supermassive black holes in*

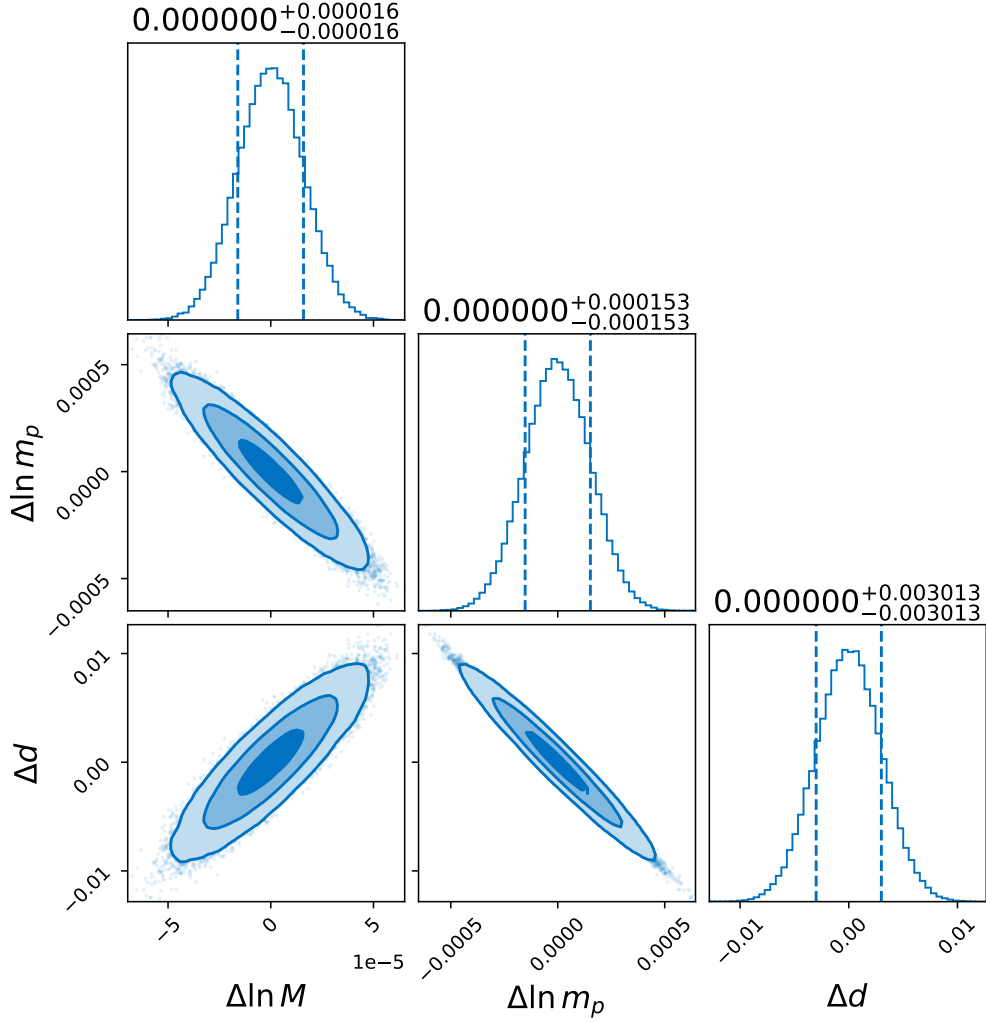


Figure 13. Corner plot for the probability distribution of the source parameters $(\ln M, \ln m_p, d)$ with LISA, inferred after one-year observations of EMRIs with $d = 0.05$ in the Schwarzschild BH background. Vertical lines show the 1σ interval for the source parameter. The contours correspond to the 68%, 95%, and 99% probability confidence intervals.

galactic nuclei, *Ann. Rev. Astron. Astrophys.* **33** (1995) 581.

- [8] K. Danzmann, *LISA: An ESA cornerstone mission for a gravitational wave observatory*, *Class. Quant. Grav.* **14** (1997) 1399.
- [9] LISA collaboration, *Laser Interferometer Space Antenna*, [1702.00786](#).
- [10] TIANQIN collaboration, *TianQin: a space-borne gravitational wave detector*, *Class. Quant. Grav.* **33** (2016) 035010 [[1512.02076](#)].
- [11] W.-R. Hu and Y.-L. Wu, *The Taiji Program in Space for gravitational wave physics and the nature of gravity*, *Natl. Sci. Rev.* **4** (2017) 685.
- [12] Y. Gong, J. Luo and B. Wang, *Concepts and status of Chinese space gravitational wave detection projects*, *Nature Astron.* **5** (2021) 881 [[2109.07442](#)].
- [13] A. Maselli, N. Franchini, L. Gualtieri and T. P. Sotiriou, *Detecting scalar fields with Extreme*

- Mass Ratio Inspirals*, *Phys. Rev. Lett.* **125** (2020) 141101 [2004.11895].
- [14] A. Maselli, N. Franchini, L. Gualtieri, T. P. Sotiriou, S. Barsanti and P. Pani, *Detecting fundamental fields with LISA observations of gravitational waves from extreme mass-ratio inspirals*, *Nature Astron.* **6** (2022) 464 [2106.11325].
- [15] N. Yunes, P. Pani and V. Cardoso, *Gravitational Waves from Quasicircular Extreme Mass-Ratio Inspirals as Probes of Scalar-Tensor Theories*, *Phys. Rev. D* **85** (2012) 102003 [1112.3351].
- [16] N. Dai, Y. Gong, T. Jiang and D. Liang, *Intermediate mass-ratio inspirals with dark matter minispikes*, *Phys. Rev. D* **106** (2022) 064003 [2111.13514].
- [17] C. Zhang and Y. Gong, *Detecting electric charge with extreme mass ratio inspirals*, *Phys. Rev. D* **105** (2022) 124046 [2204.08881].
- [18] D. Liang, R. Xu, Z.-F. Mai and L. Shao, *Probing vector hair of black holes with extreme-mass-ratio inspirals*, *Phys. Rev. D* **107** (2023) 044053 [2212.09346].
- [19] C. Zhang, H. Guo, Y. Gong and B. Wang, *Detecting vector charge with extreme mass ratio inspirals onto Kerr black holes*, [2301.05915](#).
- [20] H. Guo, C. Zhang, Y. Liu, R.-H. Yue, Y. Gong and B. Wang, *Detecting the secondary spin with extreme mass ratio inspirals in Scalar-Tensor theory*, [2305.00652](#).
- [21] D. M. Eardley, *Observable effects of a scalar gravitational field in a binary pulsar*, *Astrophys. J.* **196** (1975) L59.
- [22] C. M. Will, *Gravitational Radiation from Binary Systems in Alternative Metric Theories of Gravity: Dipole Radiation and the Binary Pulsar*, *Astrophys. J.* **214** (1977) 826.
- [23] C. Brans and R. H. Dicke, *Mach's principle and a relativistic theory of gravitation*, *Phys. Rev.* **124** (1961) 925.
- [24] R. H. Dicke, *Mach's principle and invariance under transformation of units*, *Phys. Rev.* **125** (1962) 2163.
- [25] J. Alsing, E. Berti, C. M. Will and H. Zanglauer, *Gravitational radiation from compact binary systems in the massive Brans-Dicke theory of gravity*, *Phys. Rev. D* **85** (2012) 064041 [1112.4903].
- [26] T. Damour and G. Esposito-Farese, *Tensor - scalar gravity and binary pulsar experiments*, *Phys. Rev. D* **54** (1996) 1474 [gr-qc/9602056].
- [27] M. Saijo, H.-a. Shinkai and K.-i. Maeda, *Gravitational waves in Brans-Dicke theory : Analysis by test particles around a Kerr black hole*, *Phys. Rev. D* **56** (1997) 785 [gr-qc/9701001].
- [28] J. M. Gerard and Y. Wiaux, *Gravitational dipole radiations from binary systems*, *Phys. Rev. D* **66** (2002) 024040 [gr-qc/0109062].
- [29] K. Yagi, L. C. Stein and N. Yunes, *Challenging the Presence of Scalar Charge and Dipolar Radiation in Binary Pulsars*, *Phys. Rev. D* **93** (2016) 024010 [1510.02152].
- [30] C. M. Will and H. W. Zanglauer, *Gravitational Radiation, Close Binary Systems, and the Brans-dicke Theory of Gravity*, *Astrophys. J.* **346** (1989) 366.
- [31] M. Brunetti, E. Coccia, V. Fafone and F. Fucito, *Gravitational wave radiation from compact binary systems in the Jordan-Brans-Dicke theory*, *Phys. Rev. D* **59** (1999) 044027 [gr-qc/9805056].
- [32] A. H. Mroue, H. P. Pfeiffer, L. E. Kidder and S. A. Teukolsky, *Measuring orbital eccentricity and periastron advance in quasi-circular black hole simulations*, *Phys. Rev. D* **82** (2010) 124016 [1004.4697].

- [33] L. Gondán, B. Kocsis, P. Raffai and Z. Frei, *Accuracy of Estimating Highly Eccentric Binary Black Hole Parameters with Gravitational-Wave Detections*, *Astrophys. J.* **855** (2018) 34 [[1705.10781](#)].
- [34] L. Gondán and B. Kocsis, *Measurement Accuracy of Inspiring Eccentric Neutron Star and Black Hole Binaries Using Gravitational Waves*, *Astrophys. J.* **871** (2019) 178 [[1809.00672](#)].
- [35] M. E. Lower, E. Thrane, P. D. Lasky and R. Smith, *Measuring eccentricity in binary black hole inspirals with gravitational waves*, *Phys. Rev. D* **98** (2018) 083028 [[1806.05350](#)].
- [36] I. M. Romero-Shaw, P. D. Lasky and E. Thrane, *Searching for Eccentricity: Signatures of Dynamical Formation in the First Gravitational-Wave Transient Catalogue of LIGO and Virgo*, *Mon. Not. Roy. Astron. Soc.* **490** (2019) 5210 [[1909.05466](#)].
- [37] I. M. Romero-Shaw, K. Kremer, P. D. Lasky, E. Thrane and J. Samsing, *Gravitational waves as a probe of globular cluster formation and evolution*, *Mon. Not. Roy. Astron. Soc.* **506** (2021) 2362 [[2011.14541](#)].
- [38] A. K. Lenon, A. H. Nitz and D. A. Brown, *Measuring the eccentricity of GW170817 and GW190425*, *Mon. Not. Roy. Astron. Soc.* **497** (2020) 1966 [[2005.14146](#)].
- [39] S. Wu, Z. Cao and Z.-H. Zhu, *Measuring the eccentricity of binary black holes in GWTC-1 by using the inspiral-only waveform*, *Mon. Not. Roy. Astron. Soc.* **495** (2020) 466 [[2002.05528](#)].
- [40] M. Zevin, I. M. Romero-Shaw, K. Kremer, E. Thrane and P. D. Lasky, *Implications of Eccentric Observations on Binary Black Hole Formation Channels*, *Astrophys. J. Lett.* **921** (2021) L43 [[2106.09042](#)].
- [41] A. Tucker and C. M. Will, *Residual eccentricity of inspiralling orbits at the gravitational-wave detection threshold: Accurate estimates using post-Newtonian theory*, *Phys. Rev. D* **104** (2021) 104023 [[2108.12210](#)].
- [42] T. Damour and G. Esposito-Farese, *Tensor multiscalar theories of gravitation*, *Class. Quant. Grav.* **9** (1992) 2093.
- [43] T. Damour and G. Esposito-Farese, *Gravitational wave versus binary - pulsar tests of strong field gravity*, *Phys. Rev. D* **58** (1998) 042001 [[gr-qc/9803031](#)].
- [44] J. Antoniadis et al., *A Massive Pulsar in a Compact Relativistic Binary*, *Science* **340** (2013) 6131 [[1304.6875](#)].
- [45] X. Zhang, R. Niu and W. Zhao, *Constraining the scalar-tensor gravity theories with and without screening mechanisms by combined observations*, *Phys. Rev. D* **100** (2019) 024038 [[1906.10791](#)].
- [46] B. C. Seymour and K. Yagi, *Probing Massive Scalar Fields from a Pulsar in a Stellar Triple System*, *Class. Quant. Grav.* **37** (2020) 145008 [[1908.03353](#)].
- [47] T. Jiang, N. Dai, Y. Gong, D. Liang and C. Zhang, *Constraint on Brans-Dicke theory from Intermediate/Extreme Mass Ratio Inspirals with self-force method*, [2107.02700](#).
- [48] H. Guo, Y. Liu, C. Zhang, Y. Gong, W.-L. Qian and R.-H. Yue, *Detection of scalar fields by extreme mass ratio inspirals with a Kerr black hole*, *Phys. Rev. D* **106** (2022) 024047 [[2201.10748](#)].
- [49] B. A. Campbell, N. Kaloper and K. A. Olive, *Classical hair for Kerr-Newman black holes in string gravity*, *Phys. Lett. B* **285** (1992) 199.
- [50] S. Mignemi and N. R. Stewart, *Charged black holes in effective string theory*, *Phys. Rev. D* **47** (1993) 5259 [[hep-th/9212146](#)].
- [51] P. Kanti, N. E. Mavromatos, J. Rizos, K. Tamvakis and E. Winstanley, *Dilatonic black holes in higher curvature string gravity*, *Phys. Rev. D* **54** (1996) 5049 [[hep-th/9511071](#)].

- [52] N. Yunes and L. C. Stein, *Non-Spinning Black Holes in Alternative Theories of Gravity*, *Phys. Rev. D* **83** (2011) 104002 [[1101.2921](#)].
- [53] B. Kleihaus, J. Kunz and E. Radu, *Rotating Black Holes in Dilatonic Einstein-Gauss-Bonnet Theory*, *Phys. Rev. Lett.* **106** (2011) 151104 [[1101.2868](#)].
- [54] T. P. Sotiriou and S.-Y. Zhou, *Black hole hair in generalized scalar-tensor gravity*, *Phys. Rev. Lett.* **112** (2014) 251102 [[1312.3622](#)].
- [55] T. P. Sotiriou and S.-Y. Zhou, *Black hole hair in generalized scalar-tensor gravity: An explicit example*, *Phys. Rev. D* **90** (2014) 124063 [[1408.1698](#)].
- [56] G. Antoniou, A. Bakopoulos and P. Kanti, *Evasion of No-Hair Theorems and Novel Black-Hole Solutions in Gauss-Bonnet Theories*, *Phys. Rev. Lett.* **120** (2018) 131102 [[1711.03390](#)].
- [57] D. D. Doneva and S. S. Yazadjiev, *New Gauss-Bonnet Black Holes with Curvature-Induced Scalarization in Extended Scalar-Tensor Theories*, *Phys. Rev. Lett.* **120** (2018) 131103 [[1711.01187](#)].
- [58] H. O. Silva, J. Sakstein, L. Gualtieri, T. P. Sotiriou and E. Berti, *Spontaneous scalarization of black holes and compact stars from a Gauss-Bonnet coupling*, *Phys. Rev. Lett.* **120** (2018) 131104 [[1711.02080](#)].
- [59] V. Cardoso, C. F. B. Macedo and R. Vicente, *Eccentricity evolution of compact binaries and applications to gravitational-wave physics*, *Phys. Rev. D* **103** (2021) 023015 [[2010.15151](#)].
- [60] R. Nair, S. Perkins, H. O. Silva and N. Yunes, *Fundamental Physics Implications for Higher-Curvature Theories from Binary Black Hole Signals in the LIGO-Virgo Catalog GWTC-1*, *Phys. Rev. Lett.* **123** (2019) 191101 [[1905.00870](#)].
- [61] F.-L. Julié and E. Berti, *Post-Newtonian dynamics and black hole thermodynamics in Einstein-scalar-Gauss-Bonnet gravity*, *Phys. Rev. D* **100** (2019) 104061 [[1909.05258](#)].
- [62] P. Pani and V. Cardoso, *Are black holes in alternative theories serious astrophysical candidates? The Case for Einstein-Dilaton-Gauss-Bonnet black holes*, *Phys. Rev. D* **79** (2009) 084031 [[0902.1569](#)].
- [63] B. Bertotti, L. Iess and P. Tortora, *A test of general relativity using radio links with the Cassini spacecraft*, *Nature* **425** (2003) 374.
- [64] K. Yagi, *A New constraint on scalar Gauss-Bonnet gravity and a possible explanation for the excess of the orbital decay rate in a low-mass X-ray binary*, *Phys. Rev. D* **86** (2012) 081504 [[1204.4524](#)].
- [65] H.-T. Wang, S.-P. Tang, P.-C. Li, M.-Z. Han and Y.-Z. Fan, *Tight constraints on Einstein-dilation-Gauss-Bonnet gravity from GW190412 and GW190814*, *Phys. Rev. D* **104** (2021) 024015 [[2104.07590](#)].
- [66] B. Wang, C. Shi, J.-d. Zhang, Y.-M. hu and J. Mei, *Constraining the EdGB theory with higher harmonics and merger-ringdown contribution using GWTC-3*, [2302.10112](#).
- [67] S. A. Teukolsky, *Perturbations of a rotating black hole. 1. Fundamental equations for gravitational electromagnetic and neutrino field perturbations*, *Astrophys. J.* **185** (1973) 635.
- [68] W. H. Press and S. A. Teukolsky, *Perturbations of a Rotating Black Hole. II. Dynamical Stability of the Kerr Metric*, *Astrophys. J.* **185** (1973) 649.
- [69] S. A. Teukolsky and W. H. Press, *Perturbations of a rotating black hole. III - Interaction of the hole with gravitational and electromagnetic radiation*, *Astrophys. J.* **193** (1974) 443.
- [70] F. J. Zerilli, *Effective potential for even parity Regge-Wheeler gravitational perturbation equations*, *Phys. Rev. Lett.* **24** (1970) 737.
- [71] S. Chandrasekhar, *On the equations governing the perturbations of the Schwarzschild black hole*, *Proc. Roy. Soc. Lond. A* **343** (1975) 289.

- [72] E. Poisson, *Gravitational radiation from a particle in circular orbit around a black hole. 1: Analytical results for the nonrotating case*, *Phys. Rev. D* **47** (1993) 1497.
- [73] E. Poisson, *Gravitational radiation from a particle in circular orbit around a black hole. 6. Accuracy of the postNewtonian expansion*, *Phys. Rev. D* **52** (1995) 5719 [[gr-qc/9505030](#)].
- [74] T. Apostolatos, D. Kennefick, E. Poisson and A. Ori, *Gravitational radiation from a particle in circular orbit around a black hole. 3: Stability of circular orbits under radiation reaction*, *Phys. Rev. D* **47** (1993) 5376.
- [75] C. Cutler, D. Kennefick and E. Poisson, *Gravitational radiation reaction for bound motion around a Schwarzschild black hole*, *Phys. Rev. D* **50** (1994) 3816.
- [76] S. Barsanti, N. Franchini, L. Gualtieri, A. Maselli and T. P. Sotiriou, *Extreme mass-ratio inspirals as probes of scalar fields: Eccentric equatorial orbits around Kerr black holes*, *Phys. Rev. D* **106** (2022) 044029 [[2203.05003](#)].
- [77] M. L. Katz, A. J. K. Chua, L. Speri, N. Warburton and S. A. Hughes, *Fast extreme-mass-ratio-inspiral waveforms: New tools for millihertz gravitational-wave data analysis*, *Phys. Rev. D* **104** (2021) 064047 [[2104.04582](#)].
- [78] D. M. Eardley, *Observable effects of a scalar gravitational field in a binary pulsar.*, *Astrophys. J.* **196** (1975) L59.
- [79] F.-L. Julié, *Reducing the two-body problem in scalar-tensor theories to the motion of a test particle : a scalar-tensor effective-one-body approach*, *Phys. Rev. D* **97** (2018) 024047 [[1709.09742](#)].
- [80] F.-L. Julié, *On the motion of hairy black holes in Einstein-Maxwell-dilaton theories*, *JCAP* **01** (2018) 026 [[1711.10769](#)].
- [81] L. Lindblom, B. J. Owen and D. A. Brown, *Model Waveform Accuracy Standards for Gravitational Wave Data Analysis*, *Phys. Rev. D* **78** (2008) 124020 [[0809.3844](#)].
- [82] A. J. K. Chua and J. R. Gair, *Improved analytic extreme-mass-ratio inspiral model for scoping out eLISA data analysis*, *Class. Quant. Grav.* **32** (2015) 232002 [[1510.06245](#)].
- [83] N. Warburton and L. Barack, *Self force on a scalar charge in Kerr spacetime: eccentric equatorial orbits*, *Phys. Rev. D* **83** (2011) 124038 [[1103.0287](#)].
- [84] A. J. K. Chua, M. L. Katz, N. Warburton and S. A. Hughes, *Rapid generation of fully relativistic extreme-mass-ratio-inspiral waveform templates for LISA data analysis*, *Phys. Rev. Lett.* **126** (2021) 051102 [[2008.06071](#)].
- [85] L. C. Stein and N. Warburton, *Location of the last stable orbit in Kerr spacetime*, *Phys. Rev. D* **101** (2020) 064007 [[1912.07609](#)].
- [86] K. Chatzioannou, A. Klein, N. Yunes and N. Cornish, *Constructing Gravitational Waves from Generic Spin-Precessing Compact Binary Inspirals*, *Phys. Rev. D* **95** (2017) 104004 [[1703.03967](#)].
- [87] A. Ohashi, H. Tagoshi and M. Sasaki, *PostNewtonian expansion of gravitational waves from a compact star orbiting a rotating black hole in Brans-Dicke theory: Circular orbit case*, *Prog. Theor. Phys.* **96** (1996) 713.
- [88] H. Tagoshi, *PostNewtonian expansion of gravitational waves from a particle in slightly eccentric orbit around a rotating black hole*, *Prog. Theor. Phys.* **93** (1995) 307.